Atmos. Chem. Phys. Discuss., https://doi.org/10.5194/acp-2017-1176
Manuscript under review for journal Atmos. Chem. Phys.
Discussion started: 18 December 2017

Ozone seasonal evolution and photochemical production regime in polluted troposphere in eastern China derived from high resolution FTS observations

Youwen Sun$^{1, 2)\#}$, Cheng Liu $^{2, 3, 1)\#*}$, Mathias Palm $^{4)}$, Corinne Vigouroux $^{5)}$, Qihou Hu $^{1)}$, Yuan Tian$^{1)}$, Wei Wang $^{1)}$, Wenjing Su $^{3)}$, Wenqiang Zhang $^{3)}$, Changong Shan $^{1)}$, Xingwei, Xu$^{1)}$, Jianguo Liu $^{1)}$, Justus Notholt $^{4)}$ and Martine De Mazière $^{5)}$

(1 *Key Laboratory of Environmental Optics and Technology, Anhui Institute of Optics and Fine Mechanics, Chinese Academy of Sciences, Hefei 230031, China*)

(2 *Center for Excellence in Urban Atmospheric Environment, Institute of Urban Environment, Chinese Academy of Sciences, Xiamen 361021, China*)

(3 *University of Science and Technology of China, Hefei, 230026, China*)

(4 *University of Bremen, Institute of Environmental Physics, P. O. Box 330440, 28334 Bremen, Germany*)

(5 *Royal Belgian Institute for Space Aeronomy (BIRA-IASB), Brussels, Belgium*)

\# These two authors contributed equally to this work

Abstract:

A precise knowledge of ozone seasonal evolution and photochemical production regime in polluted troposphere in China has important policy implications for ozone pollution controls especially in megacities where ozone pollution is common throughout the year. In this study, we used tropospheric ozone, CO and HCHO columns derived from high resolution Fourier transform infrared spectrometry (FTS) in Hefei, China, tropospheric NO_2 columns deduced from overpass Ozone Monitoring Instrument (OMI), surface meteorological data, and a back trajectory cluster analysis technique to investigate ozone seasonal evolution and photochemical production regime in eastern China from 2014 - 2017. A pronounced seasonal cycle for tropospheric ozone is captured by FTS, where high levels of tropospheric ozone occurs in spring and summer, and low levels of tropospheric ozone occurs in autumn and winter. Day-to-day variations in spring and summer are in most cases larger than those in autumn and winter. At the same time, it shows that the tropospheric ozone

---

Correspondence to: Cheng Liu (chliu81@ustc.edu.cn)

roughly increases over time at the first half year and reaches the maximum in June, and then it decreases over time at the second half year. Tropospheric ozone columns in June are, on average, 0.5×10^{18} molecules*cm^{-2} (47.6%) higher than those in December which has a mean value of 1.05×10^{18} molecules*cm^{-2}. The OMI time series shows similar behaviour. The measured features can basically be reproduced by GEOS-Chem and WRF-Chem data but with slight shifts in the timing of the seasonal maximum. Back trajectories analysis shows that: air pollutions in megacities in central-southern China, northwest China, and the key pollution area, i.e., Yangtze River Delta area in eastern China, dominates the contributions to the observed tropospheric ozone levels, while the contributions from the other two key pollution areas, i.e., Beijing-Tianjin-Hebei in north China and Pearl River Delta in south China, are very small; Air masses generated from polluted areas have more transportations to the observed area in spring and summer than in autumn and winter, and hence have more contributions to the observed tropospheric ozone levels. Correlations between tropospheric ozone and meteorological data disclosed that spring and summer is more favorable to photochemical ozone production than in autumn and winter. Finally, the $HCHO/NO_2$ ratio is used as a proxy to investigate the chemical sensitivity of ozone production (PO3). The results show that the PO3 is mainly NO_x limited in summer, while it is mainly VOC or mix VOC-NO_x limited in winter. Statistics show that NO_x limited, mix VOC-NO_x limited, and VOC limited PO3 accounts for 60.1%, 28.7%, and 11%, respectively.

Key words: Tropospheric ozone, Photochemistry, NDACC, FTS

1 Introduction

Ozone in the troposphere is a key ingredient in a number of atmospheric physical and chemical processes. These include radiative forcing as ozone is an infrared absorber (greenhouse gas). It is also a precursor to the formation of the hydroxyl radical which affects the oxidizing (cleansing) capacity of the atmosphere. In addition, human health, terrestrial ecosystems, and materials degradation are impacted by poor air quality resulting from high photochemical ozone levels (Oltmans et al., 2006). In polluted areas, tropospheric ozone generates from a series of complex reactions involving CO, NO_x ($NO+NO_2$), and VOCs in the presence of sunlight (Haagen-Smit, 1952). The ozone production efficiency is nonlinearly related to concentrations of its precursors, and thus tropospheric ozone levels depend on both absolute and relative levels of NO_x and VOCs in the troposphere (Duncan et al., 2010).

Ozone production can be suppressed by reducing either emissions of NO_x or VOCs depending on it is NO_x-limited or VOC-limited photochemical regimes (Duncan et al., 1998). In order to determine the regime, the total reactivity with OH of the myriad of VOCs in the polluted area has to be estimated, as the reaction with OH is often the rate-limiting step of many oxidation pathways (Sillman, 1995; Duncan et al., 1998). In the absence of such information, the HCHO concentration can be used as a proxy for VOC reactivity because it is a short-lived oxidation product of many VOCs and is positively correlated with peroxy radicals (Duncan et al., 1998).

The global NDACC (Network for Detection of Atmospheric Composition Change, http://www.ndacc.org/) started operation in 1991 and uses high resolution Fourier transform spectrometers (FTS) to record direct sun spectra in mid-infrared (MIR) spectral range of 750 to 4200 cm^{-1} (Kurylo, 1991; Vigouroux et al., 2008; Schneider, et al., 2008; Hannigan et al., 2009; Duchatelet, et al., 2010; Sussmann, et al., 2011; Kohlhepp et al., 2011; Vigouroux et al., 2015; Wang et al., 2016). These spectra were used to retrieve time series of mixing ratio profiles for O_3, HNO_3, HCl, HF, CO, N_2O, CH_4, HCN, C_2H_6, $ClONO_2$ (Kurylo, 1991; Notholt et al., 1994) and other gases, e.g., H_2O (Palm et al., 2010), H_2O/HDO ratio (Schneider et al., 2006), OCS (Notholt, et al., 2003; Wang, et al., 2016), HCHO (Vigouroux et al., 2009), NH_3 (Paton-Walsh et al., 2005; Dammers et al., 2015) or C_2H_2, CH_3OH and HCOOH (Vigouroux et al., 2012). Most photochemical ozone production related gases can be retrieved by NDACC observations with high accuracy, and thus can be used to investigate ozone production regime.

The air suffers increasing pollution along with the development of modernization in China (https://en.wikipedia.org/wiki/China). China issued the new air quality (AQ) standard in 2013 to address current air pollution problems. Tropospheric O_3 was already included in the new AQ standard as a routine monitoring component (http://kjs.mep.gov.cn/). According to AQ data released by Chinese Ministry of Environmental Protection, tropospheric O_3 has displaced PM 2.5 as the primary pollutant in many cities during summer (http://kjs.mep.gov.cn/). High precision and accuracy of measurements for tropospheric O_3 and its precursors by FTS in China can not only improve the understanding of photochemical ozone production regime, but also greatly contribute to ozone pollution controls and the validation of satellite data and model simulations. Unfortunately, most global NDACC sites are located in Europe and Northern America, whereas the number of sites in Asia, Africa, and South America is very sparse, and there is still no NDACC station that covers the vast Chinese area (http://www.ndacc.org/).

In this study, we first investigate ozone seasonal evolution and photochemical production regime in the polluted troposphere in eastern China with tropospheric ozone, CO and HCHO derived from an FTS site in Hefei, China, tropospheric NO_2 deduced from overpass Ozone Monitoring Instrument (OMI), surface meteorological data, and the back trajectory cluster analysis technique. It is presented as follows: Section 2 presents site description and instrumentation. Section 3 investigates the possibility of the ground based FTS measurements in Hefei, China for providing reliable time series of tropospheric ozone and ozone related gases. Section 4 presents comparisons with OMI, global GEOS-Chem model simulation, and regional WRF-Chem model simulation. Section 5 investigates ozone seasonal evolution and photochemical production regime. Section 6 summarizes the conclusions.

2 Site description and instrumentation

The FTS observation site (117°10′E, 31°54′N, 30 m a.s.l. (above sea level)) is located in the western suburbs of Hefei city (the capital of Anhui Province) in central-eastern China. This site is a NDACC site candidate, its location relative to the other sites and the enlarged view is shown in Fig.1 (a). The observatory is currently the only site in China that has a continuously-operating solar FTS, making it crucial to calibrate and validate the satellite data or model simulations in this important region.

In this area prevail southeast winds in summer and northwest winds in winter. The regional landscape is mostly flat with a few hills. Downtown Hefei is located to the southeast of this site with only a 10 km distance and is densely populated with seven million people. The same as other megacities, serious air pollution is common in Hefei throughout the year (http://kjs.mep.gov.cn/). The site is surrounded by wetlands or cultivated lands in other directions. For a FTS solar absorption geometry used in NDACC, the position of the sun may affect the measurements especially for short lived compounds. Fig.1 (b) demonstrated the variations of solar zenith angle (SZA) and azimuth angle over time on a typical observation day. In the morning (sunrise), the light path travels over the downtown with a large SZA, and then decreases over time. In the afternoon (sunset), the light path gets out of the city, travels over the cultivated land or wetland, and then increases over time. Consequently, the measurements in the morning and in the afternoon would be dominated by city emissions and emissions from cultivated land or wetland, respectively. So the special observation scenario makes this site also crucial for providing data to constrain regional sources and sinks in the vicinity of Hefei city (Sun et al., 2017; Tian et al., 2017).

The observation system consists of a high resolution FTS spectrometer (IFS125HR, Bruker GmbH, Germany), a solar tracker (Tracker-A Solar 547, Bruker GmbH, Germany), and a weather station (ZENO-3200, Coastal Environmental Systems, Inc., USA). The instrument has been operating almost continuously since its installation in April 2014, and the near infrared and MIR solar spectra were alternately acquired in routine observations. The MIR spectra used in this study are recorded over a wide spectral range (about 600 – 4500 cm^{-1}) with a spectral resolution of $0.005cm^{-1}$. The instrument is equipped with a KBr beam splitter & a MCT detector for O_3 and a KBr beam splitter & an InSb detector for other gases, and it has seven optical filters to avoid detector non-linearity. The weather station includes sensors for air pressure (± 0.1hpa), air temperature (± 0.3 ° C), relative humidity (± 3%), solar radiation (± 5% under daylight spectrum conditions), wind speed (± 0.5 m/s), wind direction (± 5°), and the presence of rain.

3 FTS retrievals for ozone and ozone related gases

In order to determine tropospheric ozone seasonal evolution and photochemical production regime, tropospheric O_3, CO, NO_2, and HCHO should be known with adequate accuracy. O_3, CO and NO_2 are routinely observed in the NDACC and HCHO is currently investigated. It confirms that tropospheric O_3, CO and HCHO are robust in Hefei, but NO_2 has a low information content in the troposphere which is in good agreement with the NO_2 retrievals in other NDACC stations (Kerzenmacher et al., 2008; Robles-Gonzalez et al., 2012; Hendrick et al., 2012). So in this study, the tropospheric O_3, CO, and HCHO columns were derived from FTS measurements, while the tropospheric NO_2 columns were deduced from overpass OMI measurements.

3.1 Retrieval strategy

The latest version of SFIT4 (version 0.9.4.4) algorithm is used in the profile retrieval (http://www.ndacc.org/). Theoretical basis for SFIT4 algorithm and error analysis is described in Appendix A. The retrieval settings for O_3, CO, and HCHO are listed in Table 1. All spectroscopic line parameters are adopted from HITRAN 2008 (Rothman et al., 2009). A priori profiles of pressure, temperature and H_2O for the measurement days are interpolated from the National Centers for Environmental Protection and National Center for Atmospheric Research (NCEP/NCAR) reanalysis (Kalnay et al., 1996). A priori profiles of the target gases and the interfering gases except H_2O from a dedicated WACCM (Whole Atmosphere Community Climate Model) run. For O_3 and CO, we follow the NDACC standard convention with respect to micro windows (MWs) selection and the interfering gases consideration (https://www2.acom.ucar.edu/irwg/links; Vigouroux et al., 2008). HCHO is not yet an official NDACC species but has been retrieved at a few stations (e.g. Vigouroux et al., 2009; Jones et al., 2009; Viatte et al., 2014; Franco et al., 2015), with different retrieval settings. The four MWs used in the current study are chosen from a harmonization project taking place in view of future satellite validation (Vigouroux et al., submitted to AMT). They are centered at around 2770 cm^{-1} and the interfering gases are CH_4, O_3, N_2O, and HDO. No de-weighting signal to noise ratio (SNR) were used for O_3, while a de-weighting SNR of 500 and 600 were used for CO and HCHO, respectively. For O_3, CO, and HCHO, the interfering H_2O or HDO profile is retrieved together with the target gas profile since it almost presents in all MWs.

The selection of the regularization ($\mathbf{S}_a$ and $\mathbf{S}_\varepsilon$) is important because it impacts both retrieval and error analysis (see Appendix A). In this study, we assume $\mathbf{S}_\varepsilon$ to be diagonal for all gases, and set its diagonal elements to the inverse square of the SNR of the fitted spectra and its non-diagonal elements to zero. The diagonal elements of $\mathbf{S}_a$ represent the variability of the target gas at a given altitude, and the off diagonal elements represent the concentration correlation at different altitudes. For O_3 and HCHO, the diagonal elements of $\mathbf{S}_a$ are set to constant with altitude, with 10% and 20% variability, respectively. For CO, the diagonal elements of $\mathbf{S}_a$ correspond to 27% from ground to 34 km and decrease down to 11% at the top of atmosphere. No correlation of off diagonal matrix elements is used in all retrievals.

For all retrievals, the instrument line shape (ILS) is described with the LINEFIT14.5 output using routine HBr cell measurements (Hase et al., 1999; Hase et al., 2011).

3.2 Profile information in the FTS retrievals

The averaging kernel matrix $\mathbf{A} = d\mathbf{x\_r}/d\mathbf{x}$, with $\mathbf{x\_r}$ the retrieved profile and $\mathbf{x}$ the true profile, can be used to characterize the profile information contained in the FTS retrievals. The rows of $\mathbf{A}$ represent the sensitivity of the retrieved profile to the true profile, and are referred to as averaging kernels. Their FWHM (full width at half maximum) indicates the vertical resolution of the retrieval at a specific altitude. The area of averaging kernels represents sensitivity of the retrieval to the measurement (Rodgers, 2000). Fig. 2 shows the averaging kernels and their areas of O_3, CO, and HCHO. The altitude ranges with sensitivity larger than 0.5 and the corresponding DOFs are summarized in Table 2. Within these sensitive ranges, more than 50% of the retrieved profile information comes from measurement rather than the *a priori* information. Each gas has a different sensitive range. The sensitive range for CO and HCHO is mainly tropospheric, and for O_3 is both tropospheric and stratospheric. The typical DOFS over the total atmosphere (TC DOFS) obtained in Hefei for each gas are also included in Table 2: they are about 4.8, 3.5, and 1.2 for O_3, CO, and HCHO, respectively. They are derived from a measurement with a SZA of 43°. The 1σ standard deviations of DOFS for all measurements at different SZAs for O_3, CO, and HCHO are typically 0.3, 0.2, and 0.1, respectively.

In order to separate independent partial column amounts in retrieved profiles, we have chosen the altitude limit for each independent layer such that the DOFS in each associated partial column is not less than 1.0. Fig. 3 shows the partial column averaging kernels of O_3, CO, and HCHO within each chosen layer. Their averaging kernels are resolved at their FWHM and peak at the middle of the chosen layers. The retrieved profiles of O_3, CO, and HCHO can be divided into four, three, and one independent layers, respectively. The troposphere is well resolved by O_3, CO, and HCHO, where CO exhibits the largest resolution which contains more than two independent layers in the troposphere.

The chosen altitude ranges of the tropospheric layers for each gas and the corresponding DOFS are listed in Table 2. We have chosen the same upper limits for all gases and they are not equivalent to the real tropopause heights, but are about 3 km lower than the mean value which, derived from the NCEP database, is 15.1 km with a standard deviation (1σ) of 1.1 km for Hefei. This manner not only ensured the accuracies of tropospheric O_3, CO, and HCHO retrievals, but also minimized the influence of transport from stratosphere, i.e., the so called STE process (stratosphere-troposphere exchange).

3.3 Error analysis

Figs.4 and 5 show the error components contributing to the systematic error and random error covariance matrices of O_3, CO, and HCHO, as well as the combined errors (theoretical basis is described in Appendix A). The error profile shape reflects the propagation of different errors in the retrieval process. In the troposphere, three main sources of systematic errors for each gas are evident: smoothing error, line intensity error and line pressure broadening error. The dominant systematic error for O_3 and CO is smoothing error, and for HCHO is line intensity error. The main sources of random errors are gas dependent. The main random errors for O_3 and HCHO are measurement error, temperature profile error and interference error, and for CO are zero baseline level error, measurement error, and temperature profile error. The dominant random error for O_3 and HCHO is measurement error, and for CO is zero baseline level error. When taken all error items into account, the summarized errors in O_3, CO, and HCHO for 0 –12 km tropospheric partial column and for the total column were listed in Table 3. The total errors were calculated as the sum in quadrature of each random error and systematic error. In the troposphere associated error calculation, the elements of gain matrices were set to zero for the altitudes larger than the upper limit of tropospheric partial column (see Eqs. (A6) – (A8) in Appendix A). The total errors in the tropospheric partial columns for O_3, CO, and HCHO, have been evaluated to be 8.7%, 6.8%, and 10.2%, respectively.

4 Comparisons of FTS tropospheric ozone with satellite and model data

The FTS tropospheric O_3 data has been compared with the correlative satellite data, global chemical model data, and regional chemical model data. Our data filtering scheme, designed to minimize the impacts of significant weather events and instrument problems, is described in Appendix B. In order to accurately compare the FTS data with the correlative data, the method of Rodgers and Connor (2003) are used to consider the effects of differences in altitude grid, the *a priori* profile and vertical resolution (i.e., averaging kernel). First, the correlative ozone profiles were interpolated to the FTS altitude grid to ensure a common altitude grid. The interpolated profiles were then smoothed by the corresponding FTS averaging kernels and *a priori* profiles by Eq. (1). Finally, we compared the smoothed correlative ozone profiles with the FTS profiles.

$$\mathbf{x}_s = \mathbf{x}_a + \mathrm{A}(\mathbf{x}_c - \mathbf{x}_a) \tag{1}$$

where $\mathbf{x}_s$ represent the smoothed correlative profiles, $\mathbf{x}_a$ and $\mathbf{A}$ represent the FTS *a priori* profile and averaging kernel matrix, respectively. $\mathbf{x}_c$ is the interpolated correlative profiles. The tropospheric partial column was then calculated by integrating the smoothed profile by Eq. (2). In comparison, we have taken the FTS retrievals as the reference, and the fractional difference (**D**%) is defined here as Eq. (3),

$$PC_{trop} = \int_0^{12} \mathbf{x}_s * \mathrm{A}_m \tag{2}$$

$$\mathrm{D}\% = \frac{\mathrm{X} - \mathrm{X}_{ref}}{\mathrm{X}_{ref}} \times 100 \tag{3}$$

where $\mathbf{A}_{\mathrm{m}}$ is the air-mass profile derived from FTS retrievals. $\mathbf{X}$ is a vector which can include multiple elements such as gas profile or only one element such as tropospheric partial column. $\mathbf{X}_{ref}$ is the same as $\mathbf{X}$ but for the FTS retrievals.

In this study, the Pearson correlation coefficient (PPC) is used to measure the linear similarity or correlation between two coincident variables. We regard the two variables as completely correlated if the PCC is between 0.8 and 1.0; as well correlated if the PCC is between 0.6 and 0.8; as moderately correlated if the PCC is between 0.35 and 0.6; as weakly correlated if the PCC is between 0.2 and 0.35; and as no correlation if the PCC is between 0.0 and 0.2.

4.1 Comparison with OMI data

The FTS tropospheric ozone data were compared with the OMI PROFOZ product selected within the ± 0.7 ° latitude/longitude rectangular area around the Hefei site and with uncertainty for tropospheric ozone column of less than 10%. PROFOZ contains the retrieved ozone profile, total, stratospheric, and tropospheric ozone columns, other retrieved auxiliary parameters, random noise and total retrieval errors for all of the retrieved quantities, the retrieval averaging kernels for the ozone profile, and the random-noise measurement error covariance matrix for ozone (https://avdc.gsfc.nasa.gov/pub/data/satellite/Aura/OMI/V03/L2/OMPROFOZ/). The algorithm for OMI ozone profile retrieval has been described in detail in Liu et al. (2010). The total, stratospheric, and tropospheric ozone columns, corresponding errors are integrated from the profile and error covariance matrices.

Fig. 6 shows the comparison between the OMI and FTS retrieved ozone profiles in the troposphere from 2015 to 2017 and the corresponding fractional differences calculated using Eq. (3). FTS profiles within 3 h of OMI overpass time (13:30 local time (LT)) were averaged and used for comparison. There were 53 FTS profiles that had OMI counterparts. The smoothed profiles have much better agreement with the FTS profiles than the unsmoothed profiles. Large discrepancies between the FTS profiles and unsmoothed OMI profiles were observed especially in middle troposphere, where the fractional difference varies about 15%. However, after

Atmos. Chem. Phys. Discuss., https://doi.org/10.5194/acp-2017-1176
Manuscript under review for journal Atmos. Chem. Phys.
Discussion started: 18 December 2017

smoothing, the OMI profile is 2-13% biased lower than the FTS profile.

The coincident time series and correlation plot of tropospheric ozone column obtained by FTS and OMI are shown in Fig. 7. Both data sets are in good agreement, showing a correlation coefficient (r) of 0.73. Average difference between OMI and FTS data is -0.19×10^{17} molecules*cm^{-2}. In section 5, this difference is subtracted to minimize the difference between OMI and FTS data.

4.2 Comparison with GEOS-Chem model data

The GEOS-Chem model (v10-01, http:// wiki. seas. harvard. edu/ geos-chem/ index. php/ GEOS-Chem_v10-01) is a global 3-D chemistry transport model (CTM) driven by the GEOS-FP assimilated meteorological data from the Global Modeling Assimilation Office (GMAO) at NASA Goddard Space Flight Center. GEOS-FP is the latest meteorological data product from GMAO. The GEOS-FP 3-D products are updated every 3 h at a native horizontal resolution of 0.3125 ° longitude × 0.25 ° latitude and a 72-layer vertical grid extending to 0.01hpa (Bey et al., 2001). In this study, we simulated ozone at 2.0 ° × 2.5 ° horizontal resolution and 47 vertical pressure levels. The tagged O_3 simulation uses archived ozone production and loss rates to perform a simulation for geographically tagged ozone tracers. There needs a restart file before the tagged O_3 simulation. The initial tracer concentrations used for January 2013 were derived from a ten year spin up from the year 2004 to 2013. The outputs of GEOS-Chem simulations were ozone mixing ratio profiles cover the period from January 2013 to September 2017 with 1 h time frequency, in which the nearest grid point to FTS site coordinates were selected and interpolated to the FTS vertical grid, and then convolved with FTS averaging kernels and *a priori* profiles through Eq. (1) (Rodgers and Connor, 2003).

Fig. 8 shows the comparison between the GEOS-Chem model profiles and FTS retrieved ozone profiles in the troposphere from 2015 to 2017 and the corresponding fractional differences calculated using Eq. (3). FTS profiles within 30 min of the GEOS-Chem model time were selected for comparison. There were 481 FTS profiles that had GEOS-Chem model data counterparts. As expected, the smoothed profiles have much better agreement with the FTS profiles than the unsmoothed profiles. Large discrepancies between the FTS profiles and unsmoothed GEOS-Chem model profiles were observed especially in boundary layer and upper troposphere, where the fractional difference varies larger than 50%. However, after smoothing, the GEOS-Chem model profile is typically 13% biased lower than the FTS profile throughout the entire troposphere.

The coincident time series and correlation plot of tropospheric ozone column obtained by FTS and GEOS-Chem are shown in Fig. 9. The GEOS-Chem model data are smoother than the coincident FTS data, and the agreement of the two data sets has a correlation coefficient (r) of 0.5. Average difference between GEOS-Chem and FTS data is -0.55×10^{18} molecules*cm^{-2}. This difference is mainly attributed to the difference between GEOS-Chem input files (including ozone production and loss rates and emission inventory) and the actual ones. In section 5, we used this difference to correct the bias between GEOS-Chem and FTS data.

4.3 Comparison with WRF-Chem model data

In contrast to GEOS-Chem model, WRF-Chem is a regional and tropospheric chemical model. In this study, the WRF-Chem version 3.7 was used to simulate air pollutants and meteorological parameters. The input setting was described in detail in Liu et al.(2016). Briefly, the model domain centers at 35.0 ° N, 110.0 ° E with a grid resolution of 20×20 km and covers East China and its surrounding area. The Multi-resolution Emission Inventory for China (MEIC, http://www.meicmodel.org/) (Li et al., 2014; Liu et al., 2015) were used to provides anthropogenic emissions. The biogenic emissions were calculated online with the Model of Emissions of Gases and Aerosols from Nature (MEGAN) embedded in WRF-Chem model. WRF-Chem outputs simulations with 45 vertical layers from ground to the height of 10 hPa.

The WRF-Chem ozone profiles were also available with 1 h time frequency and treated with the same manner as that of GEOS-Chem model data. Fig. 10 shows the comparison between the WRF-Chem model profiles and FTS retrieved ozone profiles in the troposphere from 2015 to 2017 and the corresponding fractional differences calculated using Eq. (3). The discrepancies between the FTS profiles and unsmoothed WRF-Chem model profiles were observed in boundary layer and middle troposphere, and they are smaller than the discrepancies between the FTS profiles and unsmoothed GEOS-Chem model profiles. After smoothing, the difference between WRF-Chem model profile and FTS profile is typically less than 12%.

The coincident time series and correlation plot of tropospheric ozone column obtained by FTS and WRF-Chem are shown in Fig. 11. The WRF-Chem model data are smoother than the coincident FTS data, and the agreement of the two data sets has a correlation coefficient (r) of 0.65. Average difference between WRF-Chem and FTS data is -0.27×10^{18} molecules*cm^{-2}. This difference is mainly attributed to uncertainties of WRF-Chem input files including ozone production and loss rates and MEIC inventory. In section 5, we used this difference to correct the bias between WRF-Chem and FTS data.

5 Tropospheric ozone seasonal evolution and production regime

5.1 Tropospheric ozone seasonal variability

Fig.12 (a) shows the tropospheric ozone column time series recorded by FTS from 2014 to 2017. We implemented the bootstrap resampling method as described in Gardiner et al. (2008) to determine the annual trend and intra-annual variations (Gardiner et al., 2008). In the present work, we followed Gardiner's method and used a second-order Fourier series plus a linear component to determine the annual trends and intra-annual variations of tropospheric ozone at Hefei site. Even though it failed to determine the annual trend of tropospheric ozone column probably because the time series is much shorter than those in Gardiner et al. (2008), the observed seasonal cycle of tropospheric ozone variations was well captured by the bootstrap resampling method. Typically, high levels of tropospheric ozone occur in spring and summer, and low levels of tropospheric ozone occur in autumn and winter. Day-to-day variations in spring and summer are in most cases larger than those in autumn and winter. Fig. 12 (b), which shows the monthly means of tropospheric ozone columns derived from FTS, smoothed and bias corrected OMI, GEOS-Chem, and WRF-Chem data, illustrates this feature even better. At the same time, it shows that the tropospheric ozone column roughly increases over time at the first half year and reaches the maximum in June, and then it decreases over time at the second half year. Tropospheric ozone columns in June were, on average, 0.5×10^{18} molecules*cm^{-2} (47.6%) higher than those in December which has a mean value of 1.05×10^{18} molecules*cm^{-2}. The OMI time series shows similar behaviour. The measured features can basically reproduced by GEOS-Chem and WRF-Chem data but with slight shifts in the timing of the seasonal maximum.

Vigouroux et al. (2015) studied ozone trends and variability with eight global NDACC stations that have a long-term time series of FTS ozone measurements, namely, Ny-Ålesund (79 ° N), Thule (77 ° N), Kiruna (68 ° N), Harestua (60 ° N), Jungfraujoch (47 ° N), Izaña (28 ° N), Wollongong (34 ° S) and Lauder (45 ° S). All these stations were located in non-polluted or relatively clean areas. The results showed a maximum tropospheric column in spring at all stations except at Jungfraujoch which extended into summer. This is because the STE process is most effective during late winter and spring (Vigouroux et al. 2015). However, Logan (1985) observed a broad summer maximum in the mid-latitude northern hemisphere, where photochemical ozone production associated with anthropogenic sources (CO, NO_x, and VOCs) occurs. In this study, we observed a broad maximum within both spring and summer mainly because photochemical ozone production is active in both season. The selection of troposphere limit in this work minimized but cannot avoid the influence of transport from stratosphere, so the STE process may also contribute to high level of tropospheric ozone column in spring.

In order to determine where the air masses came from and thus contributed to the observed tropospheric ozone levels, we have used the HYSPLIT (Hybrid Single-Particle Lagrangian Integrated Trajectory) model to calculate the three-dimensional kinematic back trajectories (Draxler et al., 2009). In the calculation, the GDAS (University of Alaska Fairbanks GDAS Archive) meteorological fields were used with a spatial resolution of 0.25 °× 0.25 °, a time resolution of 6 h and 22 vertical levels from the surface to 250 mbar. All daily back trajectories at 12:00 UTC, with a 24 h pathway at 3000 m a.s.l., have been grouped into clusters (Stunder, 1996). The results show that, in spring and summer, air masses arriving at Hefei during 2014-2017 are 25% of east China origin, 32% of southwest China origin, 43% of northwest China origin, and with a small portion of north China origin (0.23%) (Fig. 13(a)). Air pollutions in megacities in the key pollution area, i.e., Yangtze river delta area in eastern China such as Shanghai, Nanjing, Hangzhou, Hefei, etc., central-southern China such as Changsha, Wuhan, etc., and in northwest China such as Zhenzhou, Taiyuan, etc., dominates the contribution to the observed tropospheric ozone levels in spring and summer. While the contribution from the other two key pollution areas, i.e., Beijing-Tianjin-Hebei in north China and Pearl River Delta in south China, are quite small. For west origin air masses, trajectories in autumn and winter are longer than the spring and summer ones, and the percentage increases by ~10%, where 48% of them cross northwest China and 36 % of them cross southwest China (Fig. 13(b)). As a result, air pollutions in megacities in northwest China and central-southern China in autumn and winter would contribute a little larger to the observed tropospheric ozone than in spring and summer. For east origin air masses, trajectories in autumn and winter are shorter than the spring and summer ones. Meanwhile, the direction shifts from east China to southeast China, and the percentage decreases by 10%. Thus, the air pollutions from the key Yangtze river delta area would decrease dramatically. The same as spring and summer, the air masses from north China and south China are also very small (0.28%) in autumn and winter, and thus the contribution due to air pollutions in Beijing-Tianjin-Hebei and Pearl River Delta areas are still small. Considering a fact that the air pollution in east China is typically heavier than that in west China because of densely population and industrialization, air pollutions in spring and summer in the observed area would be larger than those in autumn and winter, and thus have more contributions to the observed tropospheric ozone levels.

5.2 Monthly averaged differences

Fig.14 shows monthly (a) and seasonal (b) averaged fractional differences between FTS and the correlative data calculated from Fig.12 (b) via Eq. (3). The differences between OMI and FTS are season-independent, and they are basically consistent throughout all seasons. The differences between GEOS-Chem and FTS are season-dependent, and the differences in spring and summer are on average larger than those in winter and spring. Both positive and negative differences are observed in autumn and winter, while GEOS-Chem simulations in most cases under estimated the FTS observations in spring and summer. The differences between WRF-Chem and FTS are also season-dependent but they exhibit even clearer the features seen in the comparison between GEOS-Chem and FTS. Obviously, the differences in spring and summer are larger than those in autumn and winter, and WRF-Chem simulations under estimated the FTS observations in spring and summer.

A relatively larger difference in spring and summer for both GEOS-Chem and WRF-Chem is probably due to the two reasons: First, compared with autumn and winter, the larger air pollution in spring and summer would increase the uncertainties of emission inventories that are used as input files of model simulations. Second, ozone production is more active in spring and summer than that in autumn and winter (see section 5.3), which would increase the uncertainties of ozone production regime modeled in GEOS-Chem and WRF-Chem.

5.3 Tropospheric ozone production regime

Tropospheric ozone is not an emission pollutant, but produced by photochemical oxidation of CO, NO_x, and VOCs under certain meteorological condition. This process is complicated and thus shows regional representativeness. This section presents an investigation of the tropospheric ozone production regime in the observed area in eastern China.

Fig. 15 shows daily mean time series of temperature, pressure, humidity, wind direction, wind speed, and solar radiation recorded by the surface weather station that have tropospheric ozone counterparts. The correlation plots between FTS tropospheric ozone column and each meteorological element are shown in Fig. 16. The seasonal cycles of all coincident meteorological elements are not evident except temperature and pressure which have a clear reverse seasonal cycle, i.e., the timing of seasonal maximum and minimum is reverse. The tropospheric ozone column has moderate positive correlations with solar radiation and temperature, moderate negative correlations with pressure and humidity, and has weak negative correlations with wind direction and wind speed. As a result, spring and summer meteorological conditions are more favorable to ozone production (higher sun intensity, higher temperature and lower pressure) than in autumn and winter, which consolidates a fact that tropospheric ozone in spring and summer are larger than those in autumn and winter.

In order to determine the relationship between tropospheric ozone production and its precursors, the chemical sensitivity of ozone production (PO3) relative to CO, HCHO, and NO_2 changes was investigated. Fig. 17 shows daily mean time series of tropospheric CO, HCHO, and NO_2 columns that have tropospheric O_3 counterparts. Fig. 18 shows the correlation plot between FTS tropospheric ozone column and the coincident tropospheric CO, HCHO, and NO_2 columns. Tropospheric CO and HCHO were derived from FTS spectra as tropospheric O_3, while tropospheric NO_2 was deduced from OMI product selected within the $\pm 0.7°$ latitude/longitude rectangular area around Hefei site and with retrieval uncertainty for tropospheric column of less than 30% (https://disc.gsfc.nasa.gov/datasets/OMNO2_V003/). The same as tropospheric O_3, tropospheric HCHO exhibits a clear seasonal cycle and has a minimum in winter and maximum in summer. Pronounced tropospheric CO and NO_2 variations were observed but the seasonal cycle is not evident because both emissions are not constant over seasons. When fitting all tropospheric O_3 column to coincident CO, HCHO, and NO_2 columns, we obtained a good correlation between tropospheric O_3 and CO (Fi.g 19 (a)). However, the correlations to NO_2 (Fig. 18 (b left)) and HCHO (Fi.g 19 (c left)) were only moderate. This confirms that the observed tropospheric ozone is indeed highly correlated to air pollution, but cannot be simply attributed to either NO_x pollution or VOCs pollution.

Sillman (1995) taken HCHO and NOy (total reactive nitrogen) as the 'indicator species' and investigated the sensitivity of PO3 to changes in VOCs and NO_x, which is regarded as NO_x-limited when the ratio of HCHO to NOy is high and VOC-limited when the ratio is low. Martin et al. (2004a) and Duncan et al. (2010) extended Sillman (1995)'s technique to satellite observations, using the ratio of tropospheric HCHO to NO_2 columns (referred to as "$HCHO/NO_2$") from GOME or OMI to disclose that this diagnosis of PO3 is consistent with previous finding of surface photochemistry. Witte et al. (2011) used the extended technique to estimate changes in PO3 to the strict emission control measures (ECMs) during Beijing Summer Olympic Games period in 2008. The $HCHO/NO_2$ can be an indicator of surface photochemistry as the columns of both species are closely related to NO_x and VOC emissions due to their short lifetimes (Martin et al., 2003).

With 3-d chemical model simulations, Sillman (1995) found NO_x-limited PO3 conditions when $HCHO/NO_2$ is larger than 1.0. Martin et al. (2004a) estimated that the transition between the VOC- and NO_x-limited regimes occurs when the $HCHO/NO_2$ is ~ 1.0. Duncan et al. (2010) concluded that ozone production decreases with reductions in VOCs at $HCHO/NO_2 < 1.0$ and NO_x at $HCHO/NO_2 > 2.0$; both NO_x and VOCs reductions decrease ozone production when $HCHO/NO_2$ lies in between 1.0 and 2.0. Considering local ozone production is also influenced by other factors, such as air pollution levels and meteorological conditions (e.g., Kleinman et al., 2005), the transition threshold estimated by Sillman (1995) or Martin et al. (2004a) or Duncan et al. (2010) would vary both geographically and temporally.

Following Duncan et al. (2010)'s technique, chemical sensitivity of PO3 in Hefei was thus investigated. Since the obtainment of HCHO product was not the same as that of Duncan et al. (2010), and the air pollution and meteorological condition in Hefei were also different from those in Los Angeles. Thus, the transition thresholds ($HCHO/NO_2$ ratio at 1 and 2) are not straightly applied here. In order to determine reasonable transition thresholds, we iteratively altered the $HCHO/NO_2$ ratio threshold and judged the correlations of tropospheric O_3 to HCHO or NO_2. We found that the correlation between tropospheric O_3 and HCHO is larger than 0.6 if $HCHO/NO_2$ is less than 1.3, and the correlation between tropospheric O_3 and NO_2 is larger than 0.6 if $HCHO/NO_2$ is larger than 2.8. So we regard PO3 as VOC-limited if $HCHO/NO_2 <$ 1.3, NO_x-limited if $HCHO/NO_2 >$ 2.8, and mix VOC-NO_x-limited if $HCHO/NO_2$

Atmos. Chem. Phys. Discuss., https://doi.org/10.5194/acp-2017-1176
Manuscript under review for journal Atmos. Chem. Phys.
Discussion started: 18 December 2017

between 1.3 and 2.8. Fig. 18 (b right) exemplifies a correlation plot between O_3 and NO_2 within NO_x-limited region, and Fig. 18 (c right) exemplifies a correlation plot between O_3 and HCHO within VOC-limited region. Tropospheric O_3 shows a good correlation with both NO_2 and HCHO in the respective limited regions. With this transition criteria, 106 days of observations that have coincident O_3, HCHO, and NO_2 counterparts in the reported period are calculated. Fig. 19 (a) shows classified time series of tropospheric ozone column and HCHO/NO_2 ratios. The HCHO/NO_2 ratios in summer are typically larger than those in winter. The PO3 is mainly NO_x limited in summer, while is mainly VOC or mix VOC-NO_x limited in winter. Fig. 19 (b) listed the statistics for the 106 days of observations, which shows that NO_x limited, VOC-NO_x limited, and VOC limited PO3 accounts for 60.1%, 28.7%, and 11%, respectively. Considering most of tropospheric ozone are NO_x limited or mix VOC-NO_x limited, reductions in NO_x would reduce most tropospheric ozone in eastern China.

6 Conclusion

We have investigated the possibility of the ground based Fourier transform spectrometer (FTS) measurements in Hefei, China for providing reliable time series of tropospheric ozone and ozone related gases, CO and HCHO. The investigation showed that the FTS can retrieve robust tropospheric O_3, CO, and HCHO columns. We used the FTS tropospheric ozone to validate the Ozone Monitoring Instrument (OMI) data, global GEOS-Chem model simulation, and regional WRF-Chem simulation. The OMI time series shows a similar seasonal cycle. GEOS-Chem model and WRF-Chem model can generally reproduce the seasonal cycle observed by FTS. The agreement with OMI is better than that with GEOS-Chem model and with WRF-Chem model. Besides, the agreement with regional WRF-Chem model is better than that with global GEOS-Chem model.

We used tropospheric ozone, CO and HCHO derived from FTS measurements, tropospheric NO_2 deduced from overpass OMI, the surface meteorological data, and the back trajectory cluster analysis technique to investigate ozone seasonal evolution and photochemical production regime in eastern China from 2014 - 2017. A pronounced seasonal cycle for tropospheric ozone is observed by FTS, where high levels of tropospheric ozone occurs in spring and summer, and low levels of tropospheric ozone occurs in autumn and winter. Day-to-day variations in spring and summer are in most cases larger than those in autumn and winter. At the same time, it shows that the tropospheric ozone column increases over time at the first half year and reaches the maximum in June, and then it decreases over time at the second half year. Tropospheric ozone columns in June are, on average, 0.5×10^{18} molecules*cm^{-2} higher than those in December which has a mean value of 1.05×10^{18} molecules*cm^{-2}. The OMI time series shows similar behaviour. The measured features can basically be reproduced by GEOS-Chem and WRF-Chem data but with slight shifts in the timing of the seasonal maximum.

Back trajectories computed with the HYSPLIT show that: air pollutions in megacities in central-southern China, northwest China, and the key pollution area, i.e., Yangtze River Delta area in eastern China, dominates the contributions to the observed tropospheric ozone levels, while the contributions from the other two key pollution areas, i.e., Beijing-Tianjin-Hebei in north China and Pearl River Delta in south China, are very small; Air masses generated from polluted areas have more transportations to the observed area in spring and summer than in autumn and winter, and hence have more contributions to the observed tropospheric ozone levels. Correlations between tropospheric ozone and meteorological data disclosed that spring and summer is more sensitive to photochemical ozone production than in autumn and winter. Finally, we used the $HCHO/NO_2$ ratio as a proxy to investigate the chemical sensitivity of ozone production (PO3). The results show that the PO3 is mainly NO_x limited in summer, while it is mainly VOC or mix VOC-NO_x limited in winter. Statistics show that NO_x limited, VOC-NO_x limited, and VOC limited PO3 accounts for 60.1%, 28.7%, and 11%, respectively. Considering most of tropospheric ozone are NO_x limited or mix VOC-NO_x limited, reductions in NO_x would reduce most tropospheric ozone in Hefei.

Appendix A: Theoretical basis for retrieval and error analysis

The basic principle of SFIT4 is using an Optimal Estimation Method (OEM) to fit the calculated-to-observed spectra with an iterative Newton scheme (Rodgers, 2000; Hannigan and Coffey, 2009). The retrieved profile ***x*** is expressed as,

$$\mathrm{x}_{i+1} = \mathrm{x}_a + \mathrm{G}_y([\mathrm{y} - \mathrm{F}(\mathrm{x}_i, \mathrm{b})] + \mathrm{K}_i[\mathrm{x}_i - \mathrm{x}_a]) \quad \text{(A1)}$$

where ***x*** is retrieved profile, $\boldsymbol{x}_a$ is *a priori* profile, ***y*** is measured spectra, and **F**(***x***, **b**) is forward model calculated spectrum. The $m \times n$ matrix $\mathbf{K}_i = \Delta\mathbf{F}(\boldsymbol{x}_i, \mathbf{b})/\Delta\boldsymbol{x}_i$ is weighting function matrix or Jacobian matrix for the *i*-th iteration. $\mathbf{G}_y$ is the contribution function matrix,

$$\mathrm{G}_y = (\mathrm{K}_i^T \mathrm{S}_\varepsilon^{-1} \mathrm{K}_i^T + \mathrm{S}_a^{-1})^{-1} \mathrm{K}_i^T \mathrm{S}_\varepsilon^{-1} \quad \text{(A2)}$$

where $\mathbf{S}_\varepsilon$ and $\mathbf{S}_a$ are measurement noise covariance matrices and *a priori* profile covariance matrices, respectively. The averaging kernel matrix **A** can be calculated as (Rodgers, 2000),

$$\mathrm{A} = \mathrm{G}_y \mathrm{K} = (\mathrm{K}^T \mathrm{S}_\varepsilon^{-1} \mathrm{K}^T + \mathrm{S}_a^{-1})^{-1} \mathrm{K}^T \mathrm{S}_\varepsilon^{-1} \mathrm{K} \quad \text{(A3)}$$

The degrees of freedom for signal (DOFs) is calculated as the trace of **A**,

$$d_s = tr(\mathrm{A}) = tr((\mathrm{K}^T \mathrm{S}_\varepsilon^{-1} \mathrm{K}^T + \mathrm{S}_a^{-1})^{-1} \mathrm{K}^T \mathrm{S}_\varepsilon^{-1} \mathrm{K}) \quad \text{(A4)}$$

An error analysis and characterization is of great importance for a retrieval algorithm. Errors are traditionally classified as systematic or random according to whether they are constant between consecutive measurements, or vary randomly. The total error covariance matrix (**E**) can be expressed as the sum of the contributions from (a) the measurement error due to measurement noise ($\mathbf{E}_m$), (b) the smoothing error due to the limited altitude resolution of the FTS system ($\mathbf{E}_s$), (c) the model parameter error due to uncertainties of forward model parameters ($\mathbf{E}_{model}$), and (d) forward model error due to the error of the model in physical process simulation ($\mathbf{E}_f$):

$$\mathrm{E} = \mathrm{E}_m + \mathrm{E}_s + \mathrm{E}_{model} + \mathrm{E}_f \quad \text{(A5)}$$

The forward model error is hard to evaluate because it requires a model which includes the correct physics. In this study, we neglect the forward model error. The smoothing error $\mathbf{E}_s$ is calculated via equation (A6), the measurement error $\mathbf{E}_m$ is calculated via equation (A7), and the model parameter error $\mathbf{E}_{model}$ is calculated via equation (A8) (Rodgers, 2000).

$$\mathrm{E}_s = (\mathrm{A} - \mathrm{I})\mathrm{S}_a(\mathrm{A} - \mathrm{I})^T \quad \text{(A6)}$$

$$\mathrm{E}_m = \mathrm{G}_y \mathrm{S}_\varepsilon \mathrm{G}_y^T \quad \text{(A7)}$$

$$\mathrm{E}_{\mathrm{model}} = \mathrm{G}_y \mathrm{K}_{\mathrm{var}} \mathrm{S}_{\mathrm{var}} \mathrm{K}_{\mathrm{var}}^T \mathrm{G}_y^T \tag{A8}$$

where $\mathbf{S}_{\mathrm{var}}$ is the error covariance matrix of the model parameter vector *var*, and $\mathbf{K}_{\mathrm{var}}$ is the corresponding weighting function matrix. Here *var* refers to one of the error items listed in Table 1 except smoothing error and measurement error. In Eq. (A6), to estimate $\boldsymbol{E}_s$ correctly, $\mathbf{S}_a$ should represent natural variability of the target gas in the atmosphere, and thus should be evaluated from climatological data. In this study, the selection of $\mathbf{S}_a$ as described in Table 1 tends to underestimate the error, which is in good agreement with most similar studies. The model parameter error contains the error from retrieved parameters, namely the interference error, and the error from non-retrieved forward model parameters.

Appendix B: Data filtering

For the tropospheric O_3, CO, and HCHO columns derived from FTS measurements, we established a specific filter criterion to remove the outliers by setting certain thresholds for measurement intensity, fitting error, DOFS, and fitting residuals. Measurements satisfying the criteria as follows were classified as valid and were subsequently used in the analysis.

1) Spectra recorded with too low incident signals are discarded to ensure adequate SNRs. Meanwhile, spectra recorded with too high incident signals are discarded because of non-linearity in the detector. Specifically, for O_3 spectra recorded with MCT detector, the signal intensity should lie in between 5,000 and 11,000 ADCs, and for CO and HCHO spectra recorded with InSb detector, the signal intensity should lie in between 10,000 and 20,000 ADCs.

2) The auxiliary data such as solar intensity and meteorological data (at least surface pressure and temperature) should be recorded synchronously with the measurement. Otherwise, the measurements are screened out.

3) The observed scene must be nearly cloud-free and not seriously affected by smog or haze. The spectra recorded with a solar intensity variation (SIV) of larger than 10% were not used in this study. The SIV within the duration of a spectrum is the ratio of

the standard deviation to the average of the sun intensities.

4) The root mean square error (RMS) of the residual difference (relative difference between measured and calculated spectra after the fit) in all fitting windows has to be less than 2.5%.

5) The retrievals should be converged and the concentrations of the target and interfering gases at each sub layer should be positive.

6) The tropospheric DOFs should be larger than 0.8, the SZA should be less than 85 °.

Acknowledgements

This work is jointly supported by the National High Technology Research and Development Program of China (No. 2016YFC0200800, 2017YFC0210002, 2016YFC0203302), the National Science Foundation of China (No. 41605018, No. 41405134, No.41775025, No. 41575021, No. 51778596, No. 91544212, No. 41722501, No. 51778596), Anhui Province Natural Science Foundation of China (No. 1608085MD79), Outstanding Youth Science Foundation (No. 41722501) and the German Federal Ministry of Education and Research (BMBF) (Grant No. 01LG1214A). The processing and post processing environment for SFIT4 are provided by National Center for Atmospheric Research (NCAR), Boulder, Colorado, USA. The NDACC networks are acknowledged for supplying the SFIT software and advice. The HCHO micro-windows were obtained at BIRA-IASB during the ESA PRODEX project TROVA (2016-2018) funded by the Belgian Science Policy Office. We thank OMI science team for providing tropospheric O_3 and NO_2 products. We thank University of Wollongong for their guidance with respect to instrument alignment, site operation. The LINEFIT code is provided by Frank Hase, Karlsruhe Institute of Technology (KIT), Institute for Meteorology and Climate Research (IMK-ASF), Germany. The authors acknowledge the NOAA Air Resources Laboratory (ARL) for making the HYSPLIT transport and dispersion model available on the Internet. We thank GEOS-Chem and WRF-Chem developers for making the model available to the scientific community.

References

Bey, I., D. J. Jacob, R. M. Yantosca, J. A. Logan, B. Field, A. M. Fiore, Q. Li, H. Liu, L. J. Mickley, and M. Schultz, Global modeling of tropospheric chemistry with assimilated meteorology: Model description and evaluation, J. Geophys. Res., 106, 23,073-23,096, 2001.

Duncan, B.N., Chameides, W.L., 1998. Effects of urban emission control strategies on the export of ozone and ozone precursors from the urban atmosphere to the troposphere. J. Geophys. Res. 103 (D21), 28159-28179.

Duncan, B.N., et al., 2010. Application of OMI observations to a space-based indicator of NO_x and VOC controls on surface ozone formation. Atmos. Environ. 44, 2213-2223.

Draxler, R. R., Stunder, B., Rolph, G., and Taylor, A.: HYSPLIT_4 User's Guide, via NOAA ARL website. NOAA Air Resources Laboratory, Silver Spring, MD, December 1997, revised January 2009, http://www.arl.noaa.gov/documents/reports/hysplit_user_guide.pdf (last access: 19 May 2017), 2009.

Dammers, E., Vigouroux, C., Palm, M., Mahieu, E., Warneke, T., Smale, D., Langerock, B., Franco, B., Van Damme, M., Schaap, M., Notholt, J., and Erisman, J. W.: Retrieval of ammonia from ground-based FTIR solar spectra, Atmos. Chem. Phys. Discuss., 15, 23279-23315, doi:10.5194/acpd-15-23279-2015, 2015.

Duchatelet P., Demoulin P., Hase F., Ruhnke R., Feng W., Chipperfield M. P., Bernath P. F., Boone C. D., Walker K. A., and Mahieu E.: Hydrogen fluoride total and partial column time series above the Jungfraujoch from long term FTIR measurements: Impact of the line shape model, characterization of the error budget and seasonal cycle, and comparison with satellite and model data, J. Geophys. Res., 115, D22306, doi:10.1029/2010JD014677, 2010.

Gardiner, T., Forbes, A., de Mazière, M., Vigouroux, C., Mahieu, E., Demoulin, P., Velazco, V., Notholt, J., Blumenstock, T., Hase, F., Kramer, I., Sussmann, R., Stremme,W., Mellqvist, J., Strandberg, A., Ellingsen, K., and Gauss, M.: Trend analysis of greenhouse gases over Europe measured by a network of ground-based remote FTIR instruments, Atmos. Chem. Phys., 8, 6719–6727, doi:10.5194/acp-8-6719-2008, 2008.

Hannigan, J. and Coffey, M.: semiautonomous FTS observation system for remote sensing of stratospheric and tropospheric gases, Journal of Atmospheric and Oceanic Technology . 09/2009; 26(9). DOI: 10.1175/2009JTECHA1230.1

Haagen-Smit, A., 1952. Chemistry and physiology of Los Angeles smog. Industrial & Engineering Chemistry 44, 1342-1346.

Hase, F.: Improved instrumental line shape monitoring for the ground-based, high-resolution FTIR spectrometers of the Network for the Detection of Atmospheric Composition Change, Atmos. Meas. Tech., 5, 603–610, doi:10.5194/amt-5-603-2012,2012.

Hase, F., Blumenstock, T., and Paton-Walsh, C.: Analysis of the instrumental line shape of high-resolution Fourier transform IR spectrometers with gas cell measurements and new retrieval software, Appl. Optics, 38, 3417–3422, 1999.

Hendrick, F., Mahieu, E., Bodeker, G. E., Boersma, K. F., Chipperfield, M. P., De Mazière, M., De Smedt, I., Demoulin, P., Fayt, C., Hermans, C., Kreher, K., Lejeune, B., Pinardi, G., Servais, C., Stübi, R., van der A, R., Vernier, J.-P., and Van Roozendael, M.: Analysis of stratospheric NO_2 trends above Jungfraujoch using ground-based UV-visible, FTIR, and satellite nadir observations, Atmos. Chem. Phys., 12, 8851-8864, https://doi.org/10.5194/acp-12-8851-2012, 2012.

Kleinman, L., Daum, P., Lee, Y.-N., Nunnermacker, L., Springston, S., Weinstein-Lloyd, J., Rudolph, J., 2005. A comparative study of ozone production in five U.S.metropolitan areas. Journal of Geophysical Research 110, D02301. doi:10.1029/2004JD005096.

Kerzenmacher, T., Wolff, M. A., Strong, K., Dupuy, E., Walker, K. A., Amekudzi, L. K., Batchelor, R. L., Bernath, P. F., Berthet, G., Blumenstock, T., Boone, C. D., Bramstedt, K., Brogniez, C., Brohede, S., Burrows, J. P., Catoire, V., Dodion, J., Drummond, J. R., Dufour, D. G., Funke, B., Fussen, D., Goutail, F., Griffith, D. W. T., Haley, C. S., Hendrick, F., Höpfner, M., Huret, N., Jones, N., Kar, J., Kramer, I., Llewellyn, E. J., López-Puertas, M., Manney, G., McElroy, C. T., McLinden, C. A., Melo, S., Mikuteit, S., Murtagh, D., Nichitiu, F., Notholt, J., Nowlan, C., Piccolo, C., Pommereau, J.-P., Randall, C., Raspollini, P., Ridolfi, M., Richter, A., Schneider, M., Schrems, O., Silicani, M., Stiller, G. P., Taylor, J., Tétard, C., Toohey, M., Vanhellemont, F., Warneke, T., Zawodny, J. M., and Zou, J.: Validation of NO2 and NO from the Atmospheric Chemistry Experiment (ACE), Atmos. Chem. Phys., 8, 5801-5841, https://doi.org/10.5194/acp-8-5801-2008, 2008.

Kurylo, M. J.: Network for the detection of stratospheric change (NDSC), SPIE Proceedings 1991, P. Soc. Photo-Opt. Ins., 1491, 168–174, 1991.

Kohlhepp, R., Barthlott, S., Blumenstock, T., Hase, H., Kaiser, I., Raffalski, U., and Ruhnke, R.: Trends of HCl, $ClONO_2$, and HF column abundances from ground-based FTIR measurements in Kiruna (Sweden) in comparison with KASIMA model calculations, Atmos. Chem. Phys., 11, 4669–4677, 2011 www.atmos-chem-phys.net/11/4669/2011/doi:10.5194/acp-11-4669-2011.

Kalnay E., Kanamitsu M., Kistler R., et al. (1996) The NCEP/NCAR 40-year reanalysis project. Bulletin of the American Meteorological Society, 77, 437-472.

Li, M., Zhang, Q., Streets, D., et al., 2014.Mapping Asian anthropogenic emissions of non-methane volatile organic compounds to multiple chemical mechanisms. Atmospheric Chemistry and Physics 14, 5617-5638.

Liu, F., Zhang, Q., Tong, D., et al., 2015.High-resolution inventory of technologies, activities, and emissions of coal-fired power plants in China from 1990 to 2010. Atmospheric Chemistry and Physics 15, 13299-13317.

Liu, H., Liu, C., Xie, Z., et al., 2016.A paradox for air pollution controlling in China revealed by “APEC Blue” and “Parade Blue”. Scientific Reports 6, 34408.

Liu, X., P. K. Bhartia, K. Chance, R. J. D. Spurr, and T. P. Kurosu (2010), Ozone profile retrievals from the Ozone Monitoring Instrument, Atmos. Chem. Phys., 10, 2521-2537.

Logan, J. A.: Tropospheric Ozone: Seasonal behaviour, Trends, and Anthropogenic Influence, J. Geophys. Res., 90(D6), 10 463–10 482, 1985.

Martin, R.V., 2004. Evaluation of GOME satellite measurements of tropospheric NO and HCHO using regional data from aircraft campaigns in the southeastern United States. J. Geophys. Res. 109 (D24307). doi:10.1029/2004JD004869.

Martin, R., Jacob, D., Chance, K., Kurosu, T., Palmer, P., Evans, M., 2003. Global inventory of nitrogen dioxide emissions constrained by space-based observations of NO_2 columns. Journal of Geophysical Research 108, 4537. doi:10.1029/ 2003JD003453.

Martin, R., Fiore, A., Van Donkelaar, A., 2004a. Space-based diagnosis of surface ozone sensitivity to anthropogenic emissions. Geophysical Research Letters 31, L06120. doi:10.1029/2004GL019416.

Martin, R., Parrish, D., Ryerson, T., Nicks, D., Chance, K., Kurosu, T., Jacob, D., Sturges, E., Fried, A., Wert, B., 2004b. Evaluation of GOME satellite measurements of tropospheric NO2 and HCHO using regional data from aircraft campaigns in the southeastern United States. Journal of Geophysical Research 109, D24307. doi:10.1029/2004JD004869.

Notholt, J., Meier, A., Pfeil, S., Total Column Densities of Tropospheric and Stratospheric Trace Gases in the Undisturbed Arctic Summer Atmosphere, J. Atmos. Chem., 1995, 20, 311-332.

Notholt, J., Z. Kuang, C.P. Rinsland, G.C. Toon, M. Rex, N. Jones, T. Albrecht, H. Deckelmann, J. Krieg, C. Weinzierl, H. Bingemer, R. Weller, O. Schrems: Enhanced upper tropical tropospheric COS: Impact on the stratospheric aerosol layer, Science, 300, 307-310, 2003.

Oltmans S. J., Lefohn A. S., Harris J. M., et al. Long-term changes in tropospheric ozone. Atmospheric Environment, 2006, 40(17):3156-3173.

Palm, M. and Melsheimer, C. and Noël, S. and Heise, S. and Notholt, J. and Burrows, J. and Schrems, O.: Integrated water vapor above Ny Alesund, Spitsbergen: a multisensor intercomparison. Atmospheric Chemistry and Physics, 10 (3). pp. 1215-1226, 2010.

Paton-Walsh, C., Jones, N. B., Wilson, S. R., Haverd, V., Meier, A., Griffith, D. W. T., and Rinsland, C. P.: Measurements of trace gas emissions from Australian forest fires and correlations with coincident measurements of aerosol optical depth, J.

Geophys. Res.-Atmos., 110, 1–6, doi:10.1029/2005JD006202, 2005.

Rodgers, C. D.: Inverse methods for atmospheric sounding: Theory and Practice, Series on Atmospheric, Oceanic and Planetary Physics, Vol. 2, World Scientific Publishing Co., Singapore, 2000.

Rodgers, C. D. and Connor, B. J.: Intercomparison of remote sounding instruments, J. Geophys. Res. 108, 4116–4129, 2003.

Rothman, L. S., Gordon, I. E., Barbe, A., Benner, D. C., Bernath, P. F., Birk, M., Boudon, V., Brown, L. R., Campargue, A., Champion, J.-P., Chance, K., Coudert, L. H., Danaj, V., Devi, V. M., Fally, S., Flaud, J.-M., Gamache, R. R., Goldmanm, A., Jacquemart, D., Kleiner, I., Lacome, N., Lafferty, W. J., Mandin, J.-Y., Massie, S. T., Mikhailenko, S. N., Miller, C. E., Moazzen-Ahmadi, N., Naumenko, O. V., Nikitin, A. V., Orphal, J., Perevalov, V. I., Perrin, A., Predoi-Cross, A., Rinsland, C. P., Rotger, M., Šime. cková, M., Smith, M. A. H., Sung, K., Tashkun, S. A., Tennyson, J., Toth, R. A., Vandaele, A. C., and Vander Auwera, J.: The Hitran 2008 molecular spectroscopic database, J. Quant. Spectrosc. Ra., 110, 533–572, 2009.

Robles-Gonzalez, C., Navarro-Comas, M., Puentedura, O., Schneider, M., Hase, F., Garcia, O., Blumenstock, T., and Gil-Ojeda, M.: Intercomparison of stratospheric nitrogen dioxide columns retrieved from ground-based DOAS and FTIR and satellite DOAS instruments over the subtropical Izana station, Atmos. Meas. Tech., 9, 4471-4485, https://doi.org/10.5194/amt-9-4471-2016, 2016.

Schneider, M., Redondas, A., Hase, F., Guirado, C., Blumenstock, T., and Cuevas, E.: Comparison of ground-based Brewer and FTIR total column O_3 monitoring techniques, Atmos. Chem. Phys., 8, 5535–5550, doi:10.5194/acp-8-5535-2008, 2008.

Sussmann, R., Forster, F., Rettinger, M., and Jones, N.: Strategy for high accuracy and precision retrieval of atmospheric methane from the mid-infrared FTIR network, Atmos. Meas. Tech., 4, 1943–1964, doi:10.5194/amt-4-1943-2011, 2011.

Sun, Y., Palm, M., Weinzierl, C., Petri, C., Notholt, J., Wang, Y., and Liu, C.:

Technical note: Sensitivity of instrumental line shape monitoring for the ground-based high-resolution FTIR spectrometer with respect to different optical attenuators, Atmos. Meas. Tech., 10, 989-997, doi: 10.5194/amt-10-989-2017, 2017.

Sillman, S., 1995. The use of NOy, H2O2, and HNO3 as indicators for ozone-NO_x hydrocarbon sensitivity in urban locations. J. Geophys. Res. 100, 14175-14188.

Stunder, B.: An assessment of the Quality of Forecast Trajectories,J. Appl. Meteorol., 35, 1319–1331, 1996.

Tian Y., Sun Y.W., Liu C., Wang W., Shan C. G., Xu X.W., Hu Q.H., Characterisation of methane variability and trends from near-infrared solar spectra over Hefei, China, Atmospheric Environment, Volume 173, 2018, Pages 198-209, ISSN 1352-2310, https://doi.org/10.1016/j.atmosenv.2017.11.001.

Vigouroux, C., De Mazière, M., Demoulin, P., Servais, C., Hase, F.,Blumenstock, T., Kramer, I., Schneider, M., Mellqvist, J., Strandberg, A., Velazco, V., Notholt, J., Sussmann, R., Stremme, W., Rockmann, A., Gardiner, T., Coleman, M., and Woods, P.: Evaluation of tropospheric and stratospheric ozone trends over Western Europe from ground-based FTIR network observations, Atmos. Chem. Phys., 8, 6865–6886, 2008, http://www.atmos-chem-phys.net/8/6865/2008/.

Vigouroux, C., Stavrakou, T., Whaley, C., Dils, B., Duflot, V., Hermans, C., Kumps, N., Metzger, J.-M., Scolas, F., Vanhaelewyn, G., Müller, J.-F., Jones, D. B. A., Li, Q., and De Mazière, M.: FTIR time-series of biomass burning products (HCN, C2H6, C2H2, CH3OH, and HCOOH) at Reunion Island (21°S, 55°E) and comparisons with model data, Atmos. Chem. Phys., 12, 10367-10385, https://doi.org/10.5194/acp-12-10367-2012, 2012.

Vigouroux, C., Blumenstock, T., Coffey, M., Errera, Q., García, O., Jones, N. B., Hannigan, J. W., Hase, F., Liley, B., Mahieu, E., Mellqvist, J., Notholt, J., Palm, M., Persson, G., Schneider, M., Servais, C., Smale, D., Thölix, L., and De Mazière, M.: Trends of ozone total columns and vertical distribution from FTIR observations at eight NDACC stations around the globe, Atmos. Chem. Phys., 15, 2915-2933, doi:10.5194/acp-15-2915-2015, 2015.

Vigouroux C, Hendrick F, Stavrakou T, et al. Ground-based FTIR and MAX-DOAS observations of formaldehyde at Réunion Island and comparisons with satellite and model data[J]. Atmospheric Chemistry & Physics Discussions, 2009, 9(4):9523-9544.

Witte, J.C, Duncan, B.N, Douglass, A.R, Kurosu, T.P, Chance, K et al. "The unique OMI HCHO/NO_2 feature during the 2008 Beijing Olympics: Implications for ozone production sensitivity". Atmospheric Environment. 45.18 2011-06-01. 3103(9).

Wang, Y., Deutscher, N. M., Palm, M., Warneke, T., Notholt, J., Baker, I., Berry, J., Suntharalingam, P., Jones, N., Mahieu, E., Lejeune, B., Hannigan, J., Conway, S., Mendonca, J., Strong, K., Campbell, J. E., Wolf, A., and Kremser, S.: Towards understanding the variability in biospheric CO2 fluxes: using FTIR spectrometry and a chemical transport model to investigate the sources and sinks of carbonyl sulfide and its link to CO_2, Atmos. Chem. Phys., 16, 2123-2138, doi:10.5194/acp-16-2123-2016, 2016.

Figs

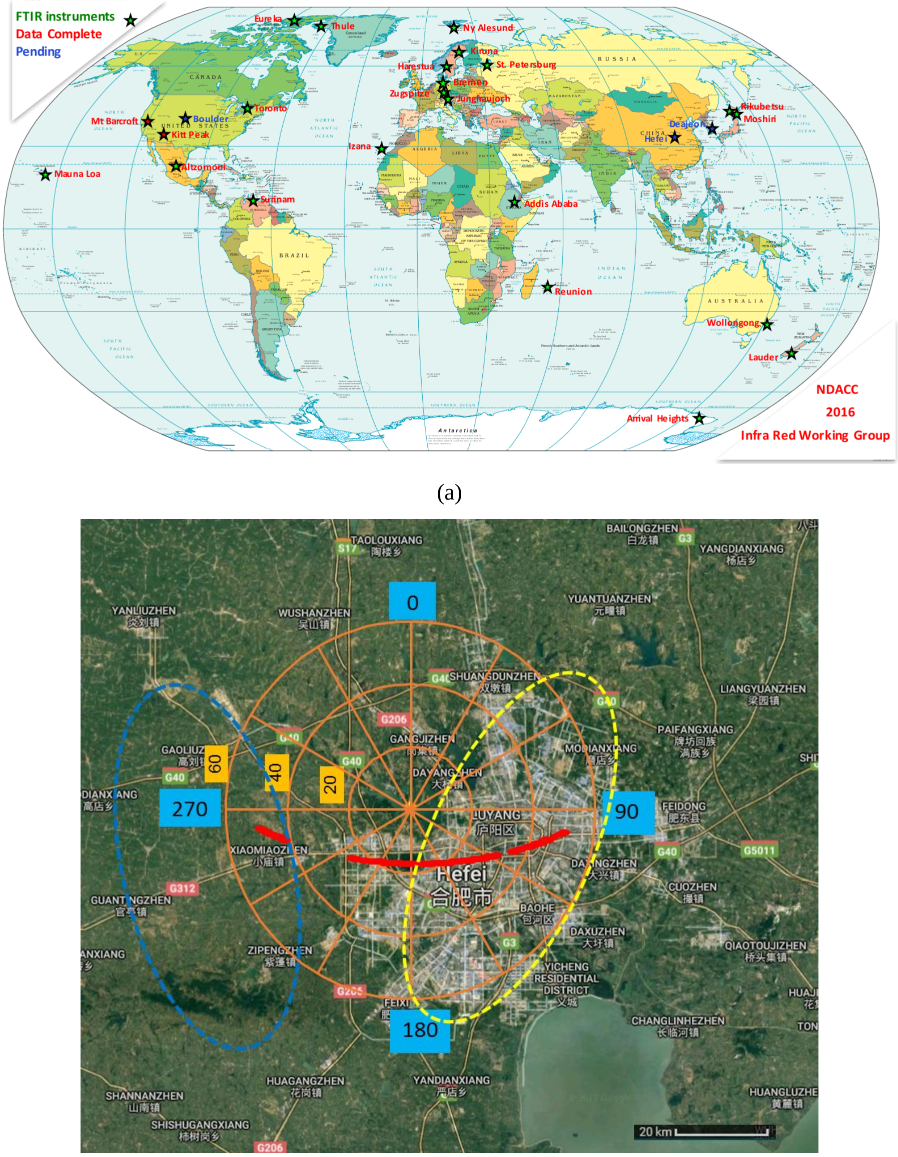

(a)

(b)

Fig.1. (a): Locations of current and pending NDACC/IRWG observation stations (http://www.ndacc.org/). (b): Enlarged view of Hefei site. The yellow dotted circle indicates the densely populated area of Hefei city (city downtown). The blue dotted circle indicates cultivated land or wetland (suburbs). The red hexagons indicate SZA and azimuth angle variations over time on a typical observation day on 14 August 2015.

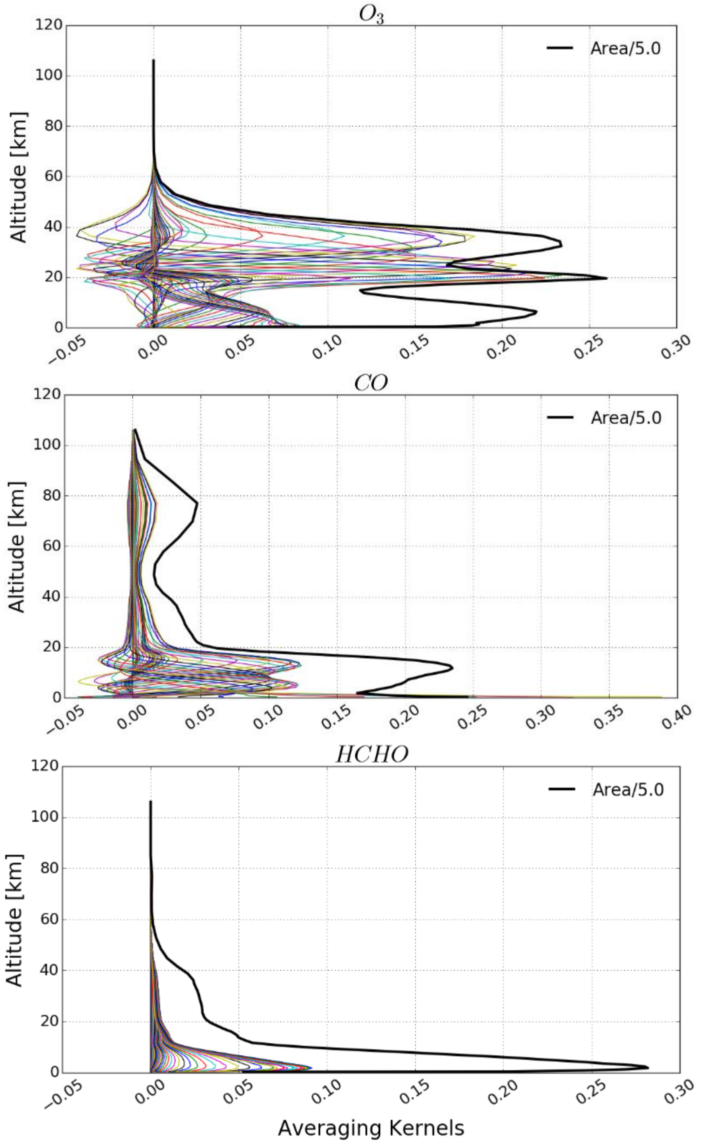

Fig.2. Averaging kernels (ppmv/ppmv) of O_3, CO, and HCHO (color fine lines), and their area scaled by a factor of 0.2 (black bold line). They are deduced from the spectra recorded in Hefei on March 15, 2016 with a measured ILS.

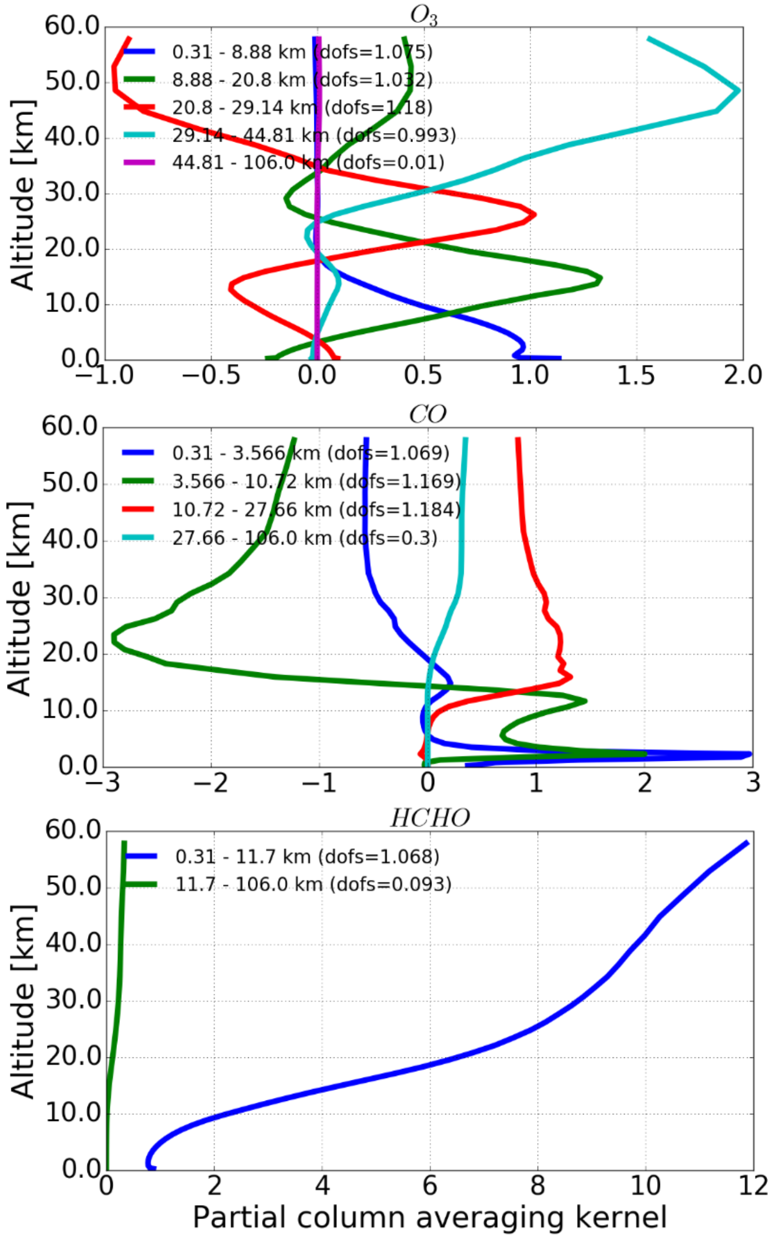

Fig.3 Partial column averaging kernels (molec cm^{-2} / molec cm^{-2}) for O_3, CO, and HCHO retrievals. For O_3 and CO, large negative PAVKs in certain altitude range are not relevant for the result because they have low content in the respective regions.

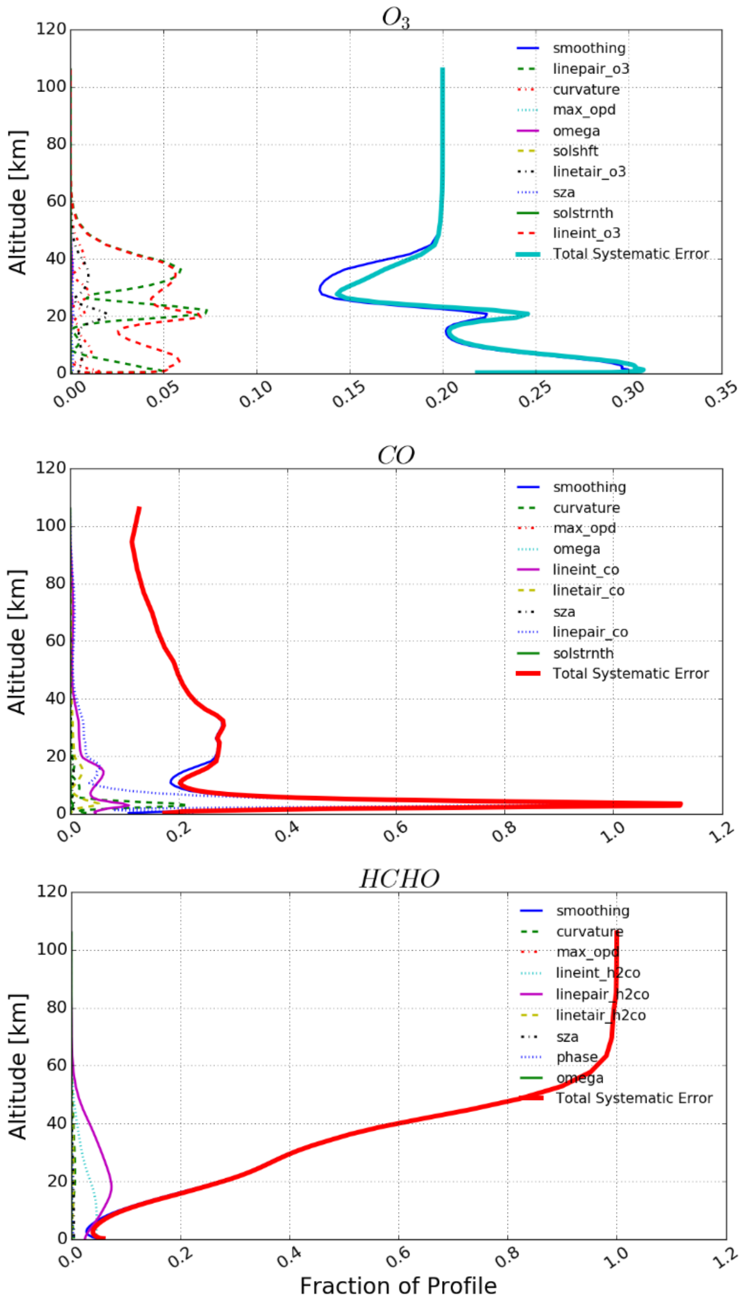

Fig.4. Ground-based FTS systematic errors for O_3, CO, and HCHO retrievals. Descriptions for the acronyms in the legend are listed in Table 1.

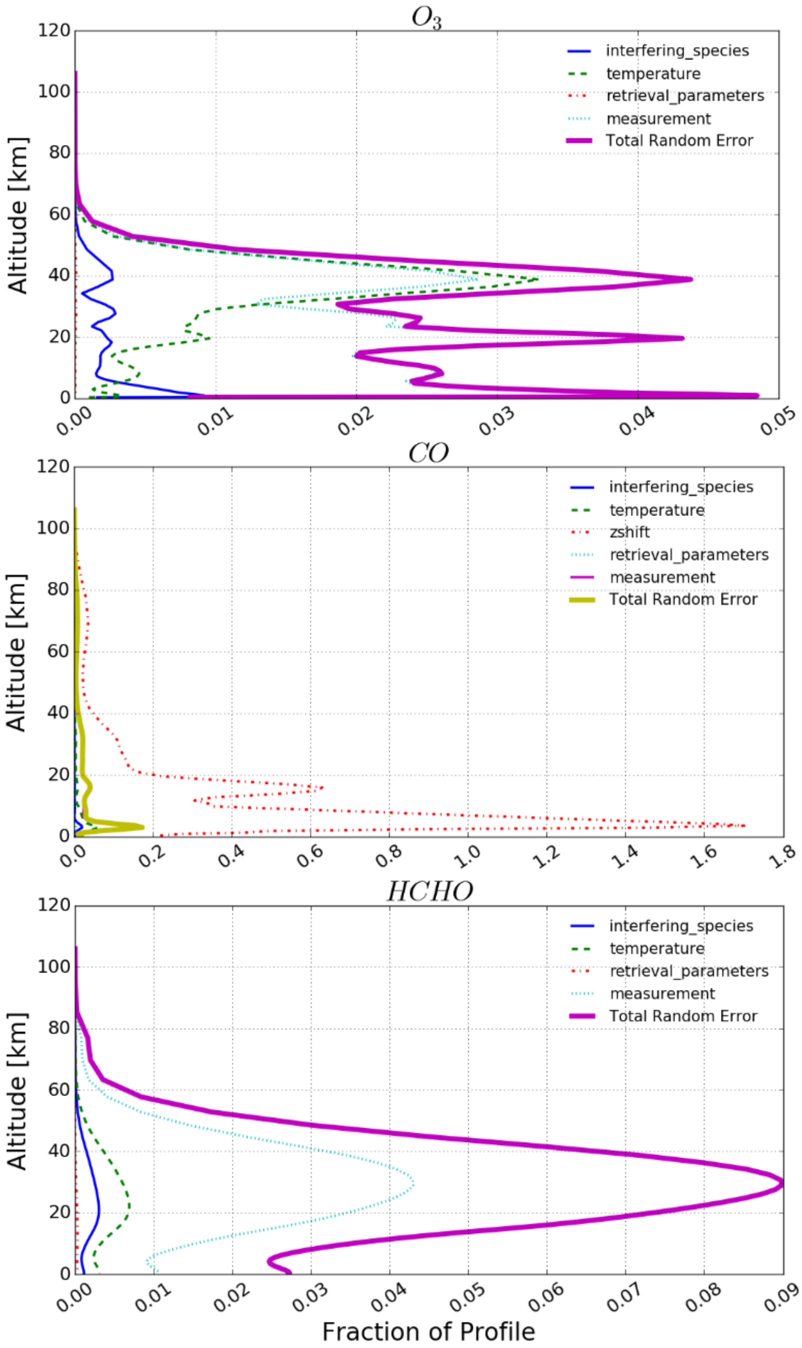

Fig.5. The same as Fig.4 but for random errors. Descriptions for the acronyms in the legend are listed in Table 1.

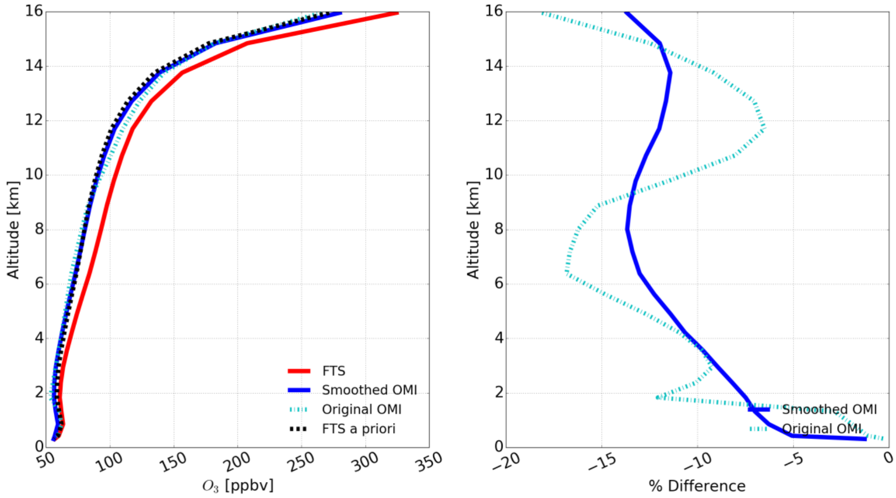

Fig.6. Left: Comparison between OMI ozone profiles and FTS ozone profiles in the troposphere during 2015 - 2017. FTS observations satisfying the criteria in Apeendix B and observation time is within 3 h of OMI overpass time (13:30 LT) were averaged and used for comparison. Red solid line shows the mean of 53 coincident FTS tropospheric profiles. Blue solid line shows the mean of 53 coincident smoothed OMI profiles. Cyan short dashed line shows the mean of 53 coincident unsmoothed OMI profiles. Black long dashed line is the *a priori* FTS profile. Right: Fractional differences between the unsmoothed OMI profile and FTS profile, and between the smoothed OMI profile and FTS profile as calculated via Eq. (3).

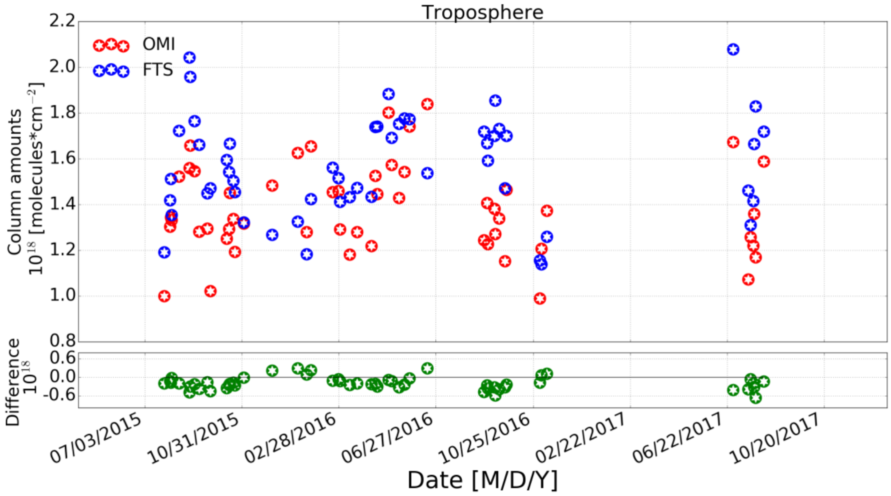

(a)

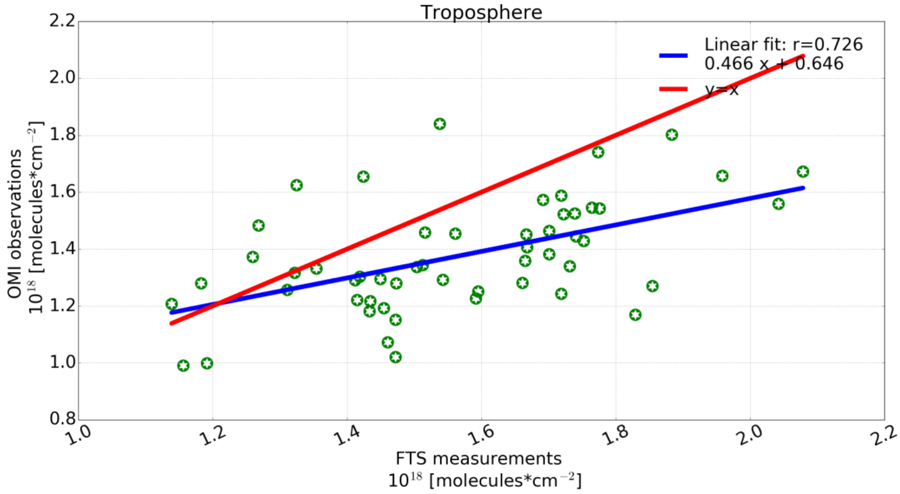

(b)

Fig.7. (a): Comparison of FTS tropospheric ozone column and smoothed OMI data. (b): Correlation plot between coincident FTS tropospheric ozone column and smoothed OMI data. The blue line is the linear fitted curve of the scatter points. The red line denotes one-to-one line.

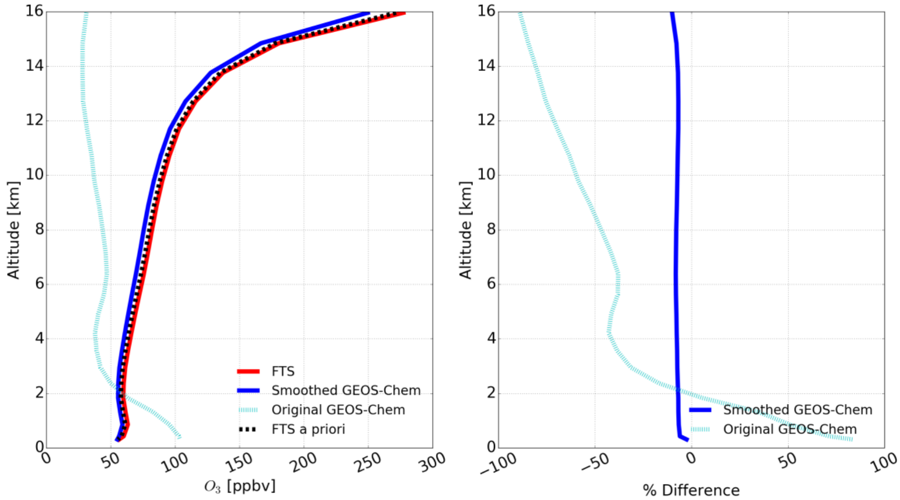

Fig.8. Left: Comparison between GEOS-Chem ozone profiles and FTS ozone profiles in the troposphere during 2015 - 2017. FTS observations satisfying the criteria in Appendix B and observation time is within 30 min of the GEOS-Chem model data were selected for the comparison. Red solid line shows the mean of 481 coincident FTS tropospheric profiles. Blue solid line shows the mean of 481 coincident smoothed GEOS-Chem model profiles. Cyan short dashed line shows the mean of 481 coincident unsmoothed GEOS-Chem model profiles. Black long dashed line is the *a priori* FTS profile. Right: Fractional differences between the unsmoothed GEOS-Chem model profile and FTS profile, and between the smoothed GEOS-Chem model profile and FTS profile as calculated via Eq. (3).

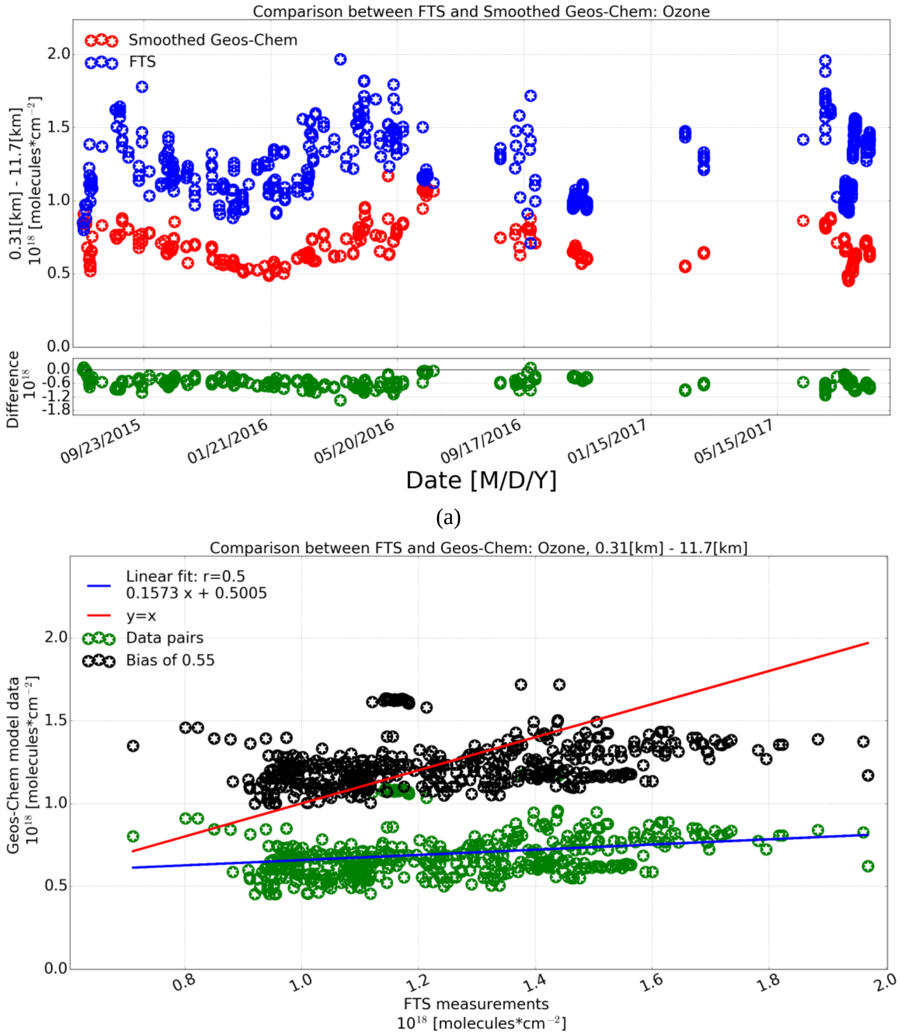

(a)

(b)

Fig.9. (a): Comparison of FTS tropospheric ozone column and smoothed GEOS-Chem model data. (b): Correlation plot between coincident FTS tropospheric ozone column and smoothed GEOS-Chem model data. The blue line is the linear fitted curve of the scatter points. The red line denotes one-to-one line. The black scatters are the same comparison but a bias of 0.55×10^{18} molecules*cm^{-2} from the smoothed GEOS-Chem model data is included.

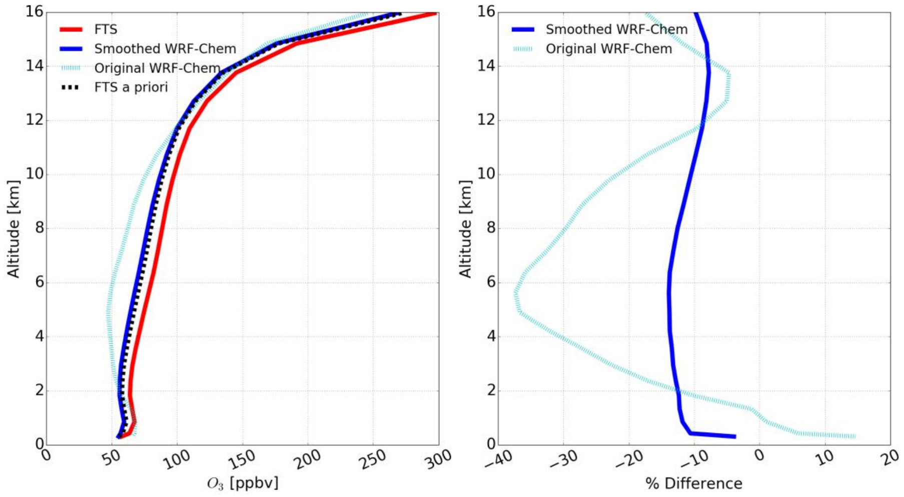

Fig.10. Left: Comparison between WRF-Chem ozone profiles and FTS ozone profiles in the troposphere during 2015 - 2017. FTS observations satisfying the criteria in Appendix B and observation time is within 30 min of the WRF-Chem model data were selected for the comparison. Red solid line shows the mean of 481 coincident FTS tropospheric profiles. Blue solid line shows the mean of 481 coincident smoothed WRF-Chem model profiles. Cyan short dashed line shows the mean of 481 coincident unsmoothed WRF-Chem model profiles. Black long dashed line is the *a priori* FTS profile. Right: Fractional differences between the unsmoothed WRF-Chem model profile and FTS profile, and between the smoothed WRF-Chem model profile and FTS profile as calculated via Eq. (3).

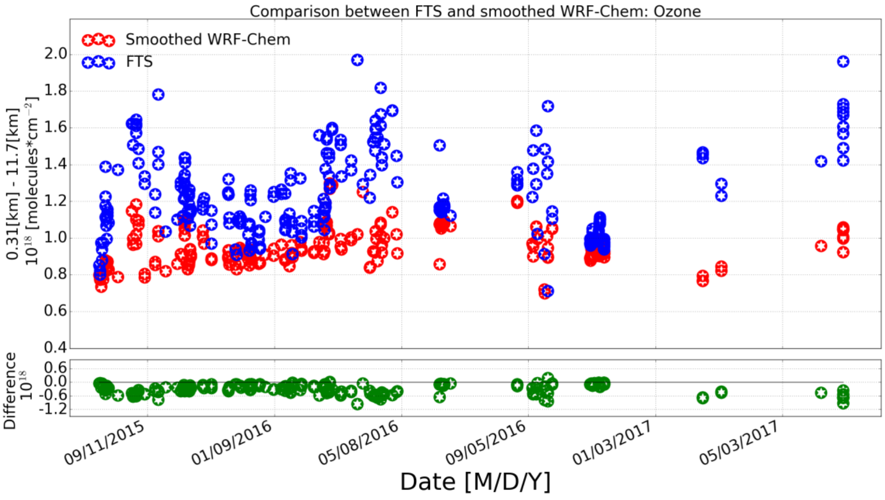

(a)

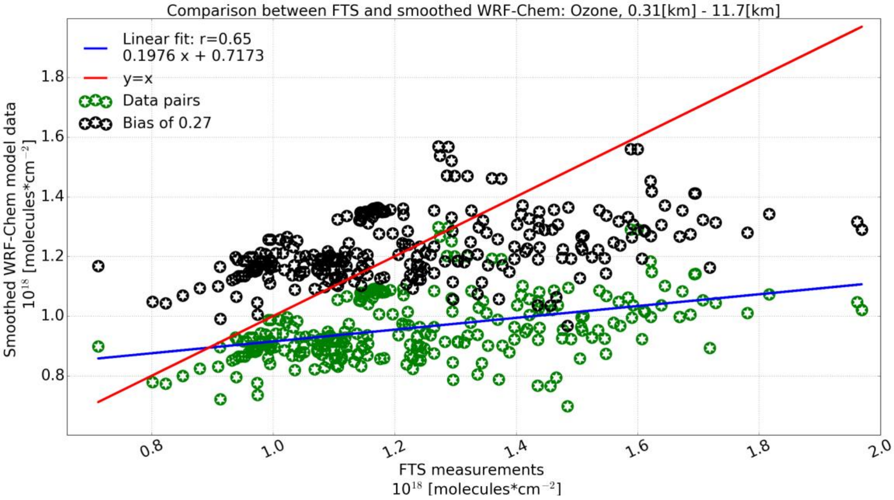

(b)

Fig.11. (a): Comparison of FTS tropospheric ozone column and smoothed WRF-Chem model data. (b): Correlation plot between coincident FTS tropospheric ozone and smoothed WRF-Chem model data. The blue line is the linear fitted curve of the scatter points. The red line denotes one-to-one line. The black scatters are the same comparison but a bias of 0.27×10^{18} molecules*cm^{-2} from the smoothed WRF-Chem model data is included.

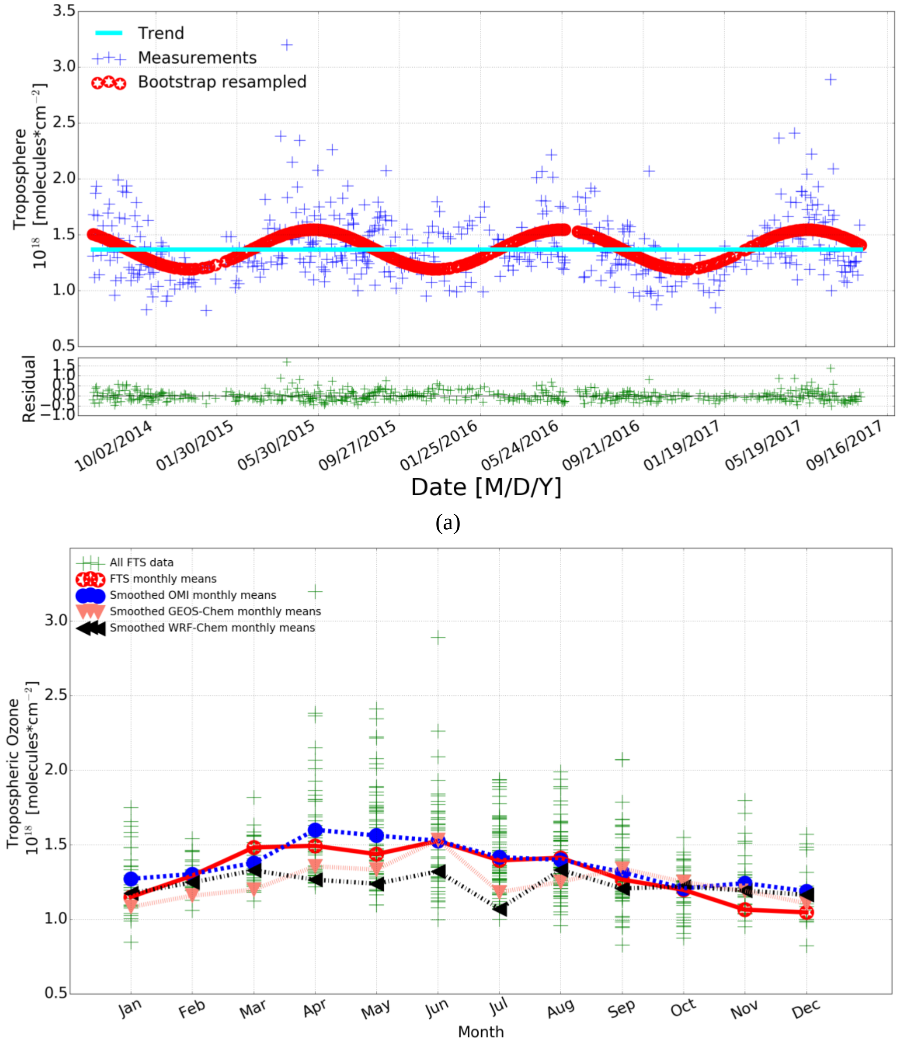

(a)

(b)

Fig.12. (a): FTS measured and bootstrap resampled tropospheric ozone partial columns at Hefei site. The linear trend and the residual are also shown. (b): Tropospheric ozone column monthly means derived from FTS, smoothed OMI, smoothed GEOS-Chem, and smoothed WRF-Chem data. Bias corrections were applied to OMI, GEOS-Chem, and WRF-Chem data with the bias constants deduced in section 4.

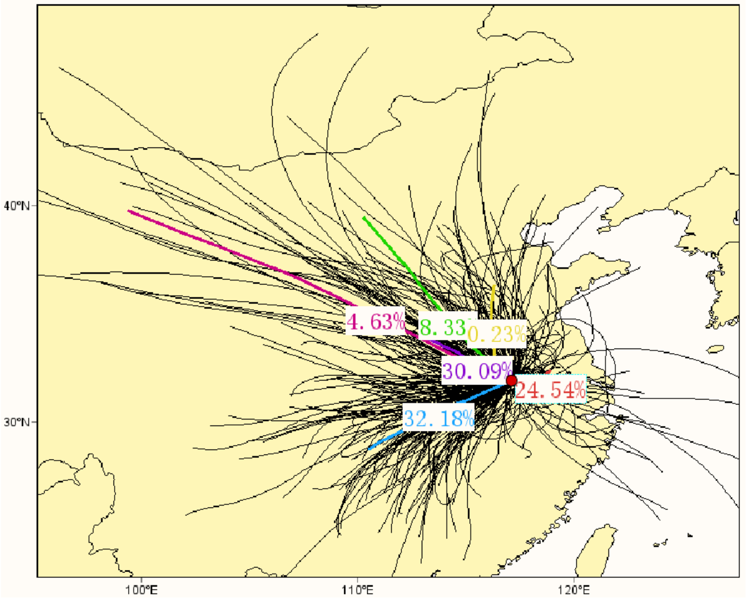

(a)

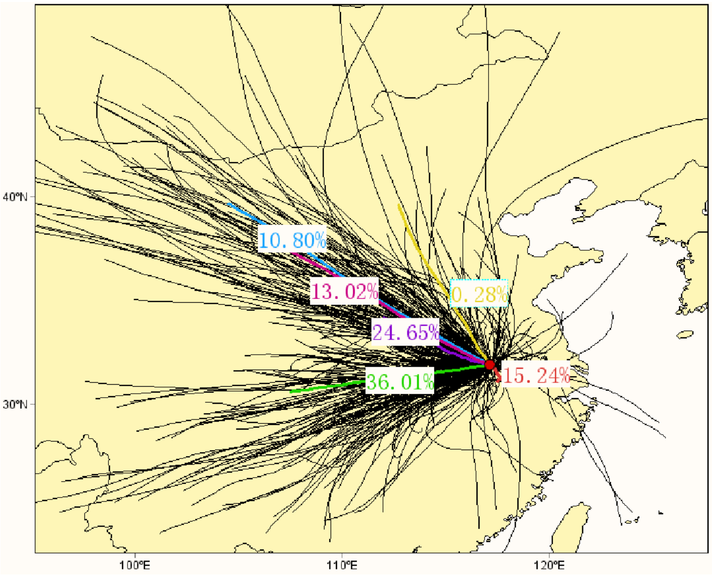

(b)

Fig.13. One-day HYSPLIT back trajectory clusters arriving at Hefei for the years 2014–2017. (a) spring and summer season, and (b) autumn and winter season.

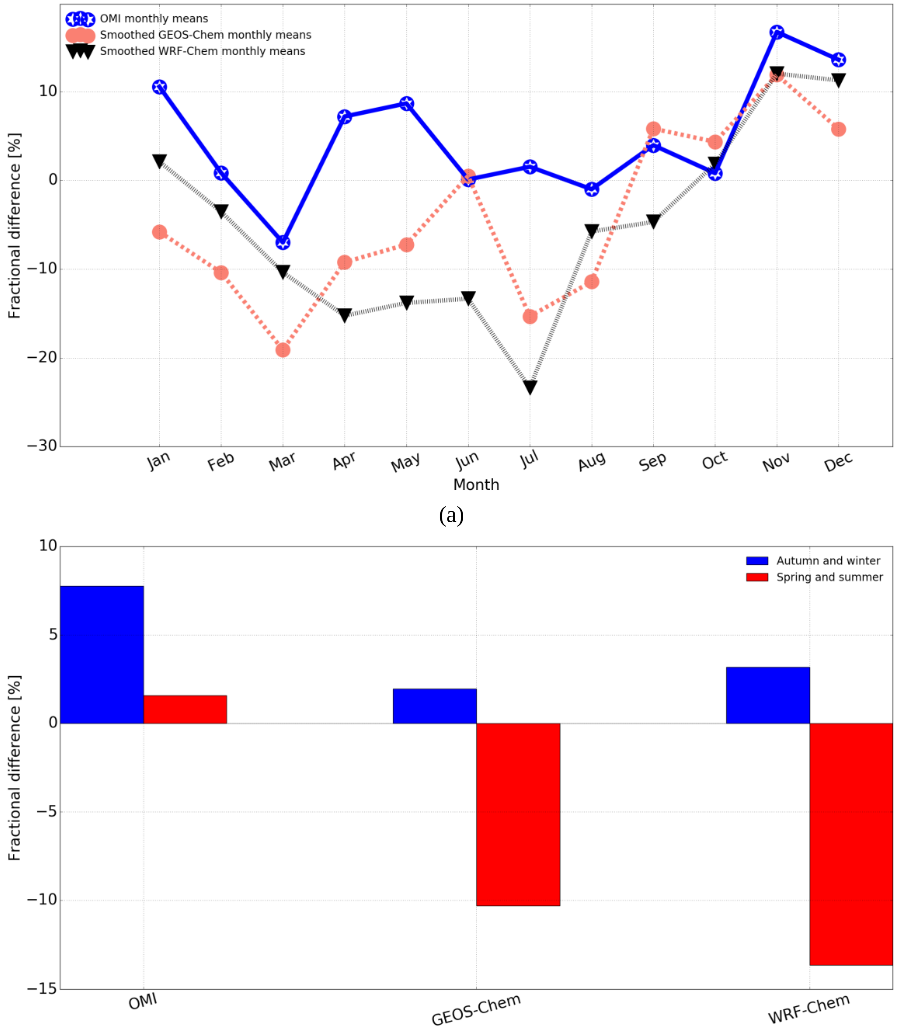

(a)

(b)

Fig. 14. (a): Monthly averaged differences calculated from Fig.13 (b) via Eq. (3). (b): Seasonal averaged differences calculated from Fig.13 (b).

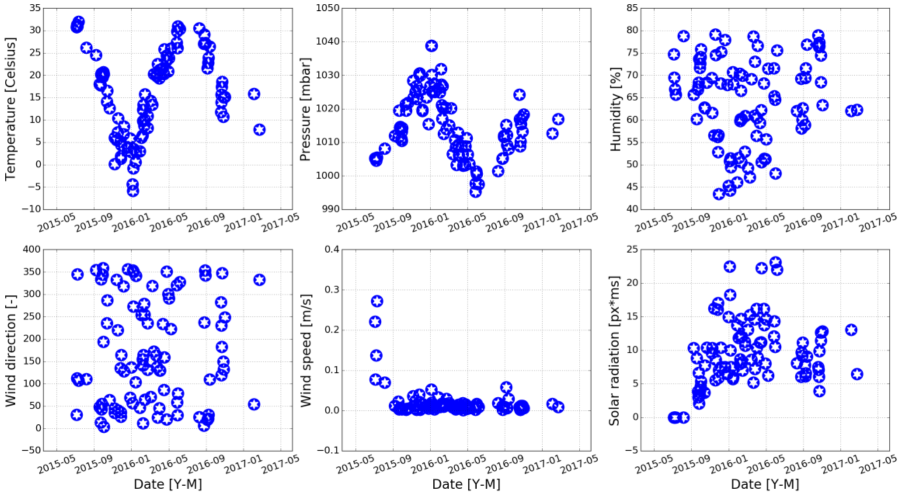

Fig.15. Daily mean time series of temperature, pressure, humidity, wind direction, wind speed, and solar radiation that have tropospheric ozone counterparts.

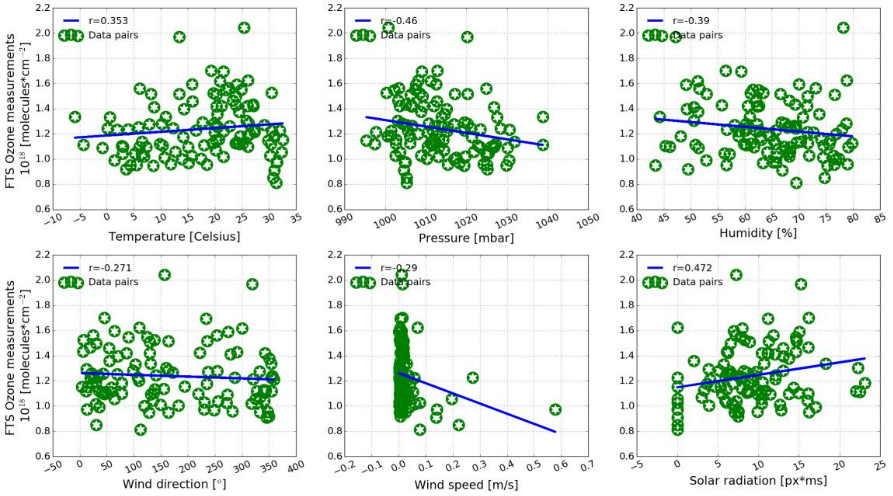

Fig.16. Correlation plot between FTS tropospheric ozone column and the coincident surface meteorological data. Temperature, pressure, humidity, wind direction, wind speed, and solar radiation are involved in the analysis.

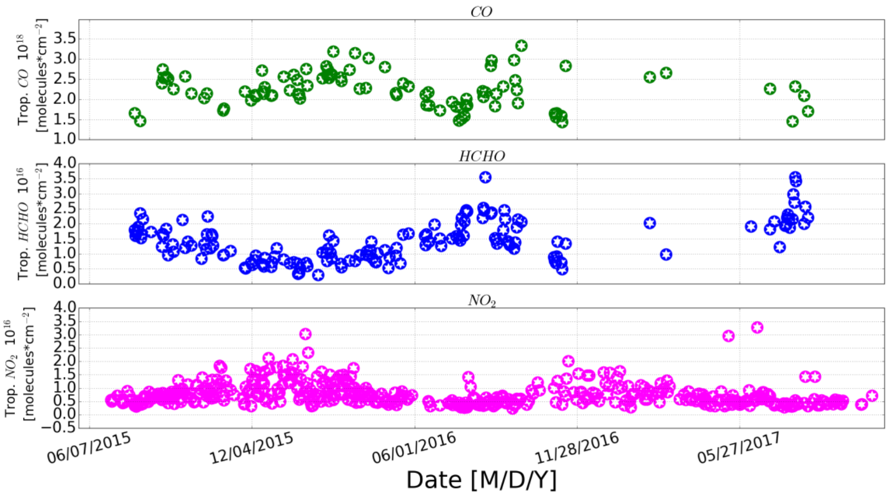

Fig.17. Time series of tropospheric CO, HCHO, and NO_2. Tropospheric CO and HCHO were derived from FTS observations as tropospheric ozone and tropospheric NO_2 is derived from OMI data.

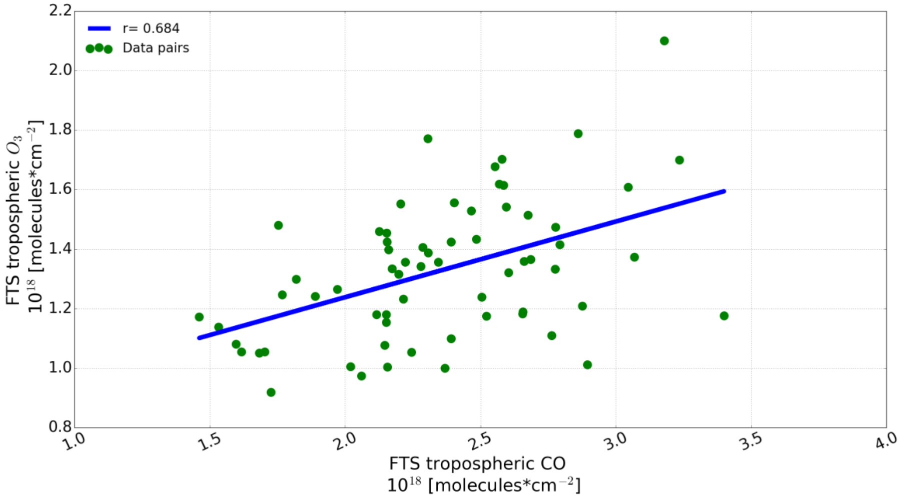

(a)

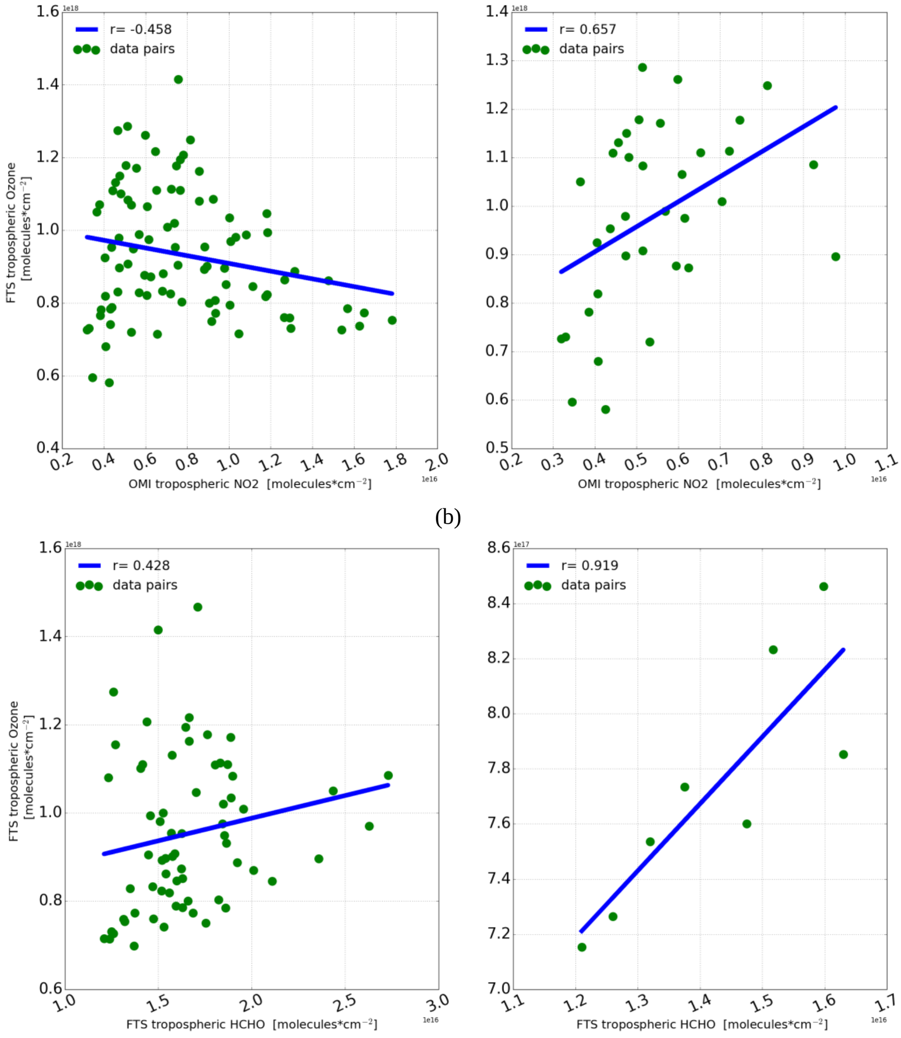

(b)

(c)

Fig.18. Correlation plots between FTS tropospheric ozone column and coincident tropospheric CO (a), NO_2 (b left), and HCHO (c left) columns. The CO and HCHO data are retrieved from FTS observations and the NO_2 data were deduced from OMI product. (b right) is the same as (b left) but only for $HCHO/NO_2 > 2.8$. (c right) is the same as (c left) but only for $HCHO/NO_2 < 1.3$.

Atmos. Chem. Phys. Discuss., https://doi.org/10.5194/acp-2017-1176
Manuscript under review for journal Atmos. Chem. Phys.
Discussion started: 18 December 2017

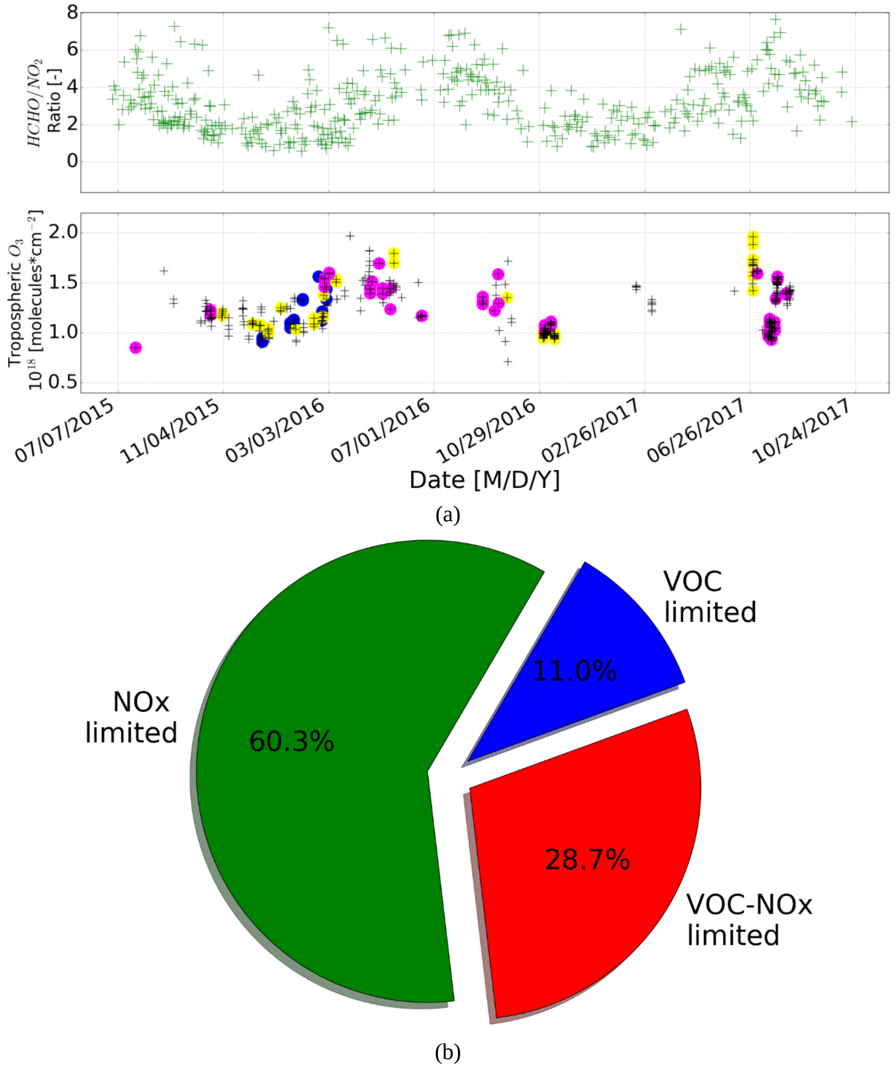

(a)

(b)

Fig.19. (a): Classified time series of tropospheric ozone column and the Formaldehyde to Nitrogen Dioxide Ratio ($HCHO/NO_2$). Magenta dots are NO_x limited, yellow dots are mix VOC-NO_x limited, and blue dots are VOC limited. (b): Proportion for chemical sensitivity of ozone production (PO3).

Tables

Table 1. Summary of the retrieval parameters used for O_3, CO, and HCHO. All micro windows (MW) are given in cm^{-1}.

Gases		O_3	CO	HCHO
Retrieval code		SFIT4 v 0.9.4.4	SFIT4 v 0.9.4.4	SFIT4 v 0.9.4.4
Spectroscopy		HITRAN2008	HITRAN2008	HITRAN2008
P, T profiles		NCEP	NCEP	NCEP
A priori profiles for target/interfering gases except H_2O		WACCM	WACCM	WACCM
MW for profile retrievals		1000-1004.5	2057.7-2058 2069.56-2069.76 2157.5-2159.15	2763.42-2764.17 2765.65-2766.01 2778.15-2779.1 2780.65-2782.0
Retrieved interfering gases		H_2O, CO_2, C_2H_4, O3668, O3686	O_3, N_2O, CO_2, OCS, H_2O	CH_4, O_3, N_2O, HDO
H_2O treatment	A priori profile	NCEP	NCEP	NCEP
	Fit in each WM	Profile retrieval	Profile retrieval	Profile retrieval
SNR for de-weighting		None	500	600
Regularization	**S_a**	Diagonal: 20% No correlation	Diagonal: 11% ~ 27% No correlation	Diagonal: 10% No correlation
	S_ε	Real SNR	Real SNR	Real SNR
ILS		LINEFIT145	LINEFIT145	LINEFIT145
Error analysis		Systematic error: -Smoothing error (smoothing) [a] -Errors from other parameters [b]: Background curvature (curvature), Optical path difference (max_opd), Field of view (omega), Solar line strength (solstrnth), Background slope (slope), Solar line shift (solshft), Phase (phase), Solar zenith angle(sza), Line temperature broadening (linetair_gas), Line pressure broadening (linepair_gas), Line intensity(lineint_gas)		
		Random error: -Interference errors: retrieval parameters (retrieval_parameters), interfering species (interfering_species) -Measurement error (measurement) - Errors from other parameters [b]: Temperature (temperature), Zero level (zshift)		

[a]The bracket shows the corresponding acronym in Figs.4 and 5; [b]The input uncertainties of all these items are the same and are included into error analysis if they are not retrieved. Otherwise, the corresponding uncertainties wouldn't be included.

Table 2. Typical degrees of freedom for signal (DOFs) and sensitive range of the retrieved O_3, CO, and HCHO profiles at Hefei site.

Gas	Total column DOFs	Sensitive range (km)	Tropospheric partial column (km)	Tropospheric DOFs
O_3	4.8	Ground - 44	Ground - 12	1.5
CO	3.5	Ground - 27	Ground - 12	2.7
HCHO	1.2	Ground - 18	Ground - 12	1.1

Table 3. Errors in % of the column amount of O_3, CO, and HCHO for 0 –12 km tropospheric partial column and for the total column.

Gas	O_3		CO		HCHO	
Altitude (km)	0 – 12	Total column	0 – 12	Total column	0 – 12	Total column
Total random	3.2	0.59	3.8	0.66	3.3	0.97
Total systematic	8.1	4.86	5.7	3.9	9.6	5.7
Total errors	8.7	5.0	6.8	3.95	10.2	5.8